

Department of Mechanical Engineering

Division of Mechanics

Lund University

ISRN LUTFD2/TFME—16/5031—SE(1-56)

Finite Element Simulations of Harmonic Structured Materials in Two Dimensions

Bachelor Dissertation by
Jakob Salomonsson

Supervisors:

Associate Professor Aylin Ahadi, Div. of Mechanics
Professor Dmytro Orlov, Div. of Materials Engineering

Copyright © 2016 by Jakob Salomonsson



For more information:
Division of Mechanics, Lund University, Box 118, SE-211 00 Lund, Sweden
Homepage: <http://www.mek.lth.se/>

Abstract

Most of today's materials show either high strength with low ductility, or relatively low strength combined with high ductility. It is strongly desired in the industry to obtain materials whose mechanical properties can display a combination of high strength and elongation. That is why the new concept of harmonic structure has been introduced recently. This structure consists of strong ultrafine grains in a uniform continuous pattern surrounding the islands of softer coarse grain.

The aim for the work presented in this dissertation was to develop a finite element model in two dimensions for harmonic structured materials to facilitate future work in this novel field. The model of harmonic structure in this work was intentionally simplified to reflect most critical structural characteristics. Subsequently, three different mesh densities were implemented.

After successful validation against existing experimental data valuable results were obtained. In consistency with experimental data obtained by other research groups, both total elongation and yield strength were extended thanks to the "harmonic" microstructure topology. The results were also found to be strongly dependent on mesh types. The finer the mesh, the lower amount of deformation was possible to apply to the model. The early model failure resulted from severe element distortion in some local areas. Important results were the uniformly distributed macro- stresses and strains along the entire model along with local shear stresses on the core/shell interface. The latter is considered to be the reason of initial cracking in the same areas reported in other publications on harmonic structured materials.

It was also shown that harmonic structured material outperforms that with a randomly distributed bimodal structure.

Acknowledgements

First of all, I would like to thank my supervisors, associate professor Aylin Ahadi and professor Dmyto Orlov, who both dedicated a lot of their time and expertise to help me solve the numerous problems that constantly emerged during the work of this project. Without their competent input this task would have taken even longer and most likely not even started. Thank you also for letting me knock on your doors at any given time when I had questions and for never hesitating to help me at these occasions.

I also want to thank Besim Ibishi, my colleague during this project, with whom I constantly discussed different approaches and who also made the entire task more joyful. Dr Mathias Agmell, who I repeatedly approached with Abaqus related questions, is definitely worth a special thanks. Last, but definitely not least, is my beloved family who supported me completely during this time. Thank you.

Contents

- 1 INTRODUCTION AND OBJECTIVE.....5**
- 2 LITERATURE REVIEW ON EARLIER RESEARCH AND BACKGROUND.....7**
- 3 THE THEORY BEHIND STRESSES, STRAINS, YIELD CRITERIA AND THE FULL NEWTON SOLUTION
TECHNIQUE REALISATION IN ABAQUS15**
 - 3.1 STRESSES AND STRAINS15
 - 3.2 YIELD CRITERIA17
 - 3.3 FULL NEWTON SOLUTION TECHNIQUE18
 - 3.4 BRIEF INTRODUCTION TO ABAQUS19
- 4 FINITE ELEMENT ANALYSIS OF HARMONIC AND HETEROGENEOUS STRUCTURES IN ABAQUS21**
 - 4.1 MODEL DEVELOPMENT.....21
 - 4.2 BOUNDARY AND INITIAL CONDITIONS.....23
 - 4.3 MATERIAL DATA24
 - 4.4 MESH DEVELOPMENT.....25
 - 4.5 HETEROGENEOUS STRUCTURE26
- 5 RESULTS AND DISCUSSIONS.....29**
 - 5.1 VERIFYING THE MODELS29
 - 5.2 VON MISES STRESS DISTRIBUTION AT LARGE SCALE.....30
 - 5.3 EQUIVALENT PLASTIC STRAIN DISTRIBUTION AT LARGE SCALE.....32
 - 5.4 STRESS AND STRAIN DISTRIBUTION AT CLOSE.....33
 - 5.5 STRESSES AND STRAINS IN X, Y AND XY DIRECTIONS38
 - 5.6 ELEMENT DEFORMATION42
 - 5.7 STRESS-STRAIN CURVES.....43
 - 5.8 HETEROGENEOUS STRUCTURE45
- 6 CONCLUSIONS AND FUTURE WORK47**
 - 6.1 CONCLUSIONS47
 - 6.2 FUTURE WORK48
- REFERENCES49**

1 Introduction and Objective

1.1 Introduction

Humans have been trying since long to obtain better materials with higher structural performance in a natural drive to outperform what they have today. Most metals nowadays are either strong with low ductility or relatively weak with long elongation. Those properties are the direct result of microstructure consisting of purely ultrafine grained or coarse grained grain size distribution. In increasingly high demands from automotive and aviation industries, among many, raising requirements for materials with a superior combination of high strength and high ductility is always a hot topic.

Recently, [1-4] a novel microstructure design named bimodal harmonic structure that combines these two highly needed mechanical properties was proposed. Such a morphology comprises of two different grain sizes distributed in a uniform pattern, as can be viewed in fig. 1.1. The coarse grained islands (or cores, light grey in fig. 1.1) are enclosed in harder ultrafine grains (black in fig. 1.1) in a three dimensional continuous constitution. Several papers on different metals have been published. They demonstrated the superior mechanical properties of harmonic structures when compared to their coarse- and ultrafine grained counterparts. Experiments have been primarily used for this research, while a finite element model is desired for the optimization of microstructure characteristics.

1.2 Objective

The aim for this project was to develop and optimize a finite element model in two dimensions that can be used to simulate the behaviour of harmonic structured materials. The numerical experiments shall be validated against existing experimental data as well as to reveal why a harmonic structure is superior to its random distributed equivalent.

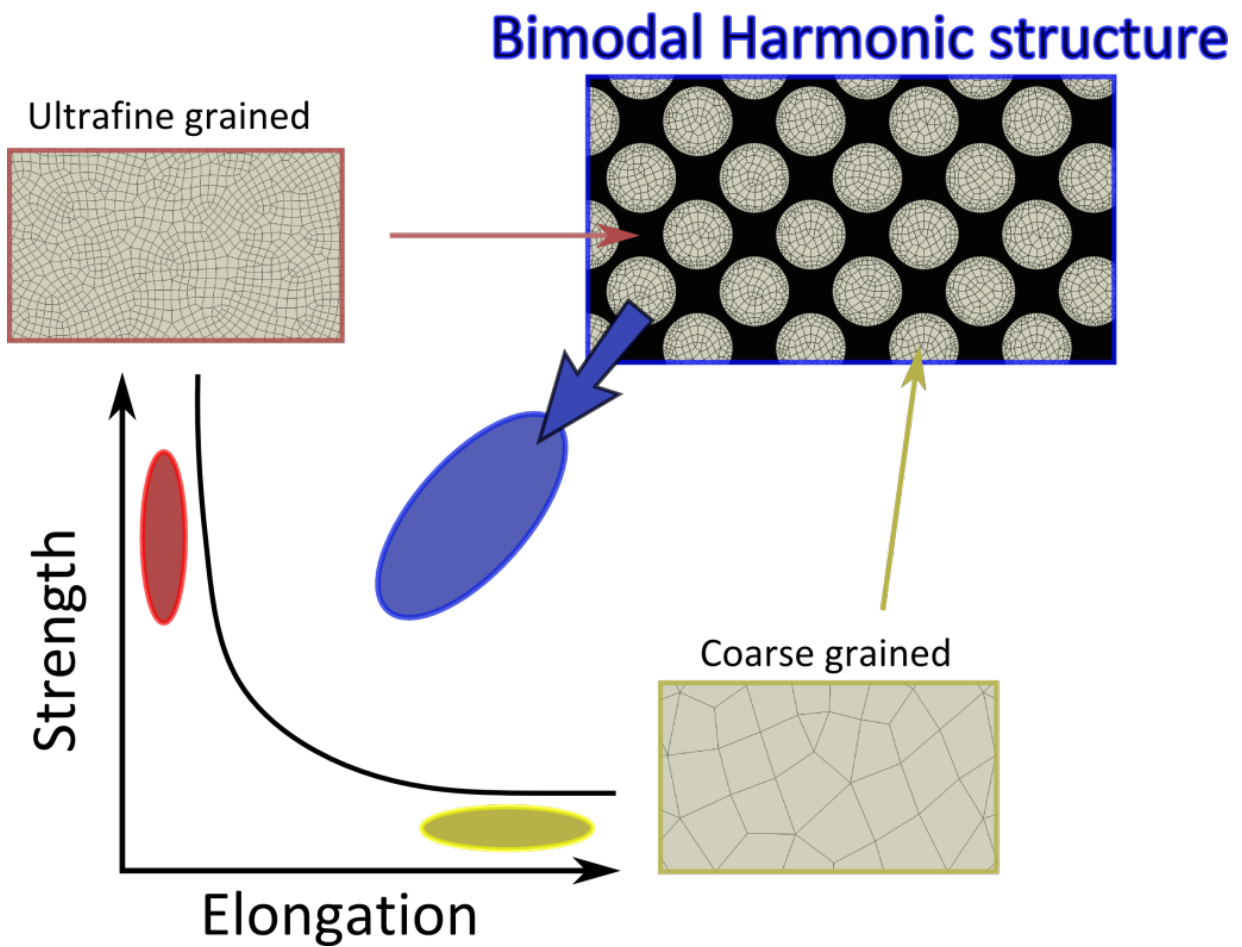


Figure 1.1 Schematic illustration of how strong, but low ductile ultrafine grain size distribution can be combined with a weaker, larger elongated coarse grained into a bimodal harmonic structure. The arrangement yields a material which mechanical properties display a combination of high strength and long elongation.

2 Literature Review on Earlier Research and Background

In this chapter a literature review is presented to demonstrate some of the research performed in the field of bimodal harmonic structure until now. Different kinds of materials are presented along with a brief overview of the finite element analysis. It is also briefly described how to fabricate such materials, so the reader can understand the motivation for this research and subsequently this dissertation.

2.1 Sawangrat et al. (2014)

Sawangrat et al. demonstrated that pure copper with a bimodal harmonic structure (HS) has an excellent combination of elongation and strength compared to its homogeneous and bimodal heterogeneous counterparts [1]. The study also revealed that the elongation and strength was proportional to the amount of ultra-fine grained (UFG) fractions in the specimen, where the optimal combination was found in the HS material with 40% UFG.

The bimodal HS consists of isolated softer coarse grained (CG) areas encompassed by hard UFG areas in an unambiguous bimodal grain size distribution. This structure was produced during several steps starting with a powder of copper having 99.96 % purity and with an average particle diameter of 160 μm . The fine particles were mechanically milled (MM) for 54 (15 h) respectively 72ks (20 h) with a balls-to-powder weight ratio of 20:1. Following this the powder was spark plasma sintered for 3.6ks (1 h) under vacuum. To evaluate the sintered material mechanical properties, tensile tests were performed at room temperature.

Furthermore, by scanning electron microscopy (SEM) and electron backscatter diffraction (EBSD) the microstructural attributes were investigated. Figure 2.1 displays the cross sections of the initial powder before milling (Fig. 2.1a), milling after 54ks (Fig. 2.1b) and (Fig. 2.1c) after 72ks. First of all, it is quite clear that before milling the microstructure consists of more or less equal sized grains. Nevertheless, after 54ks of MM the outer boarder, or “shell” area, of the particles have undergone sever plastic deformation where the grain size has greatly

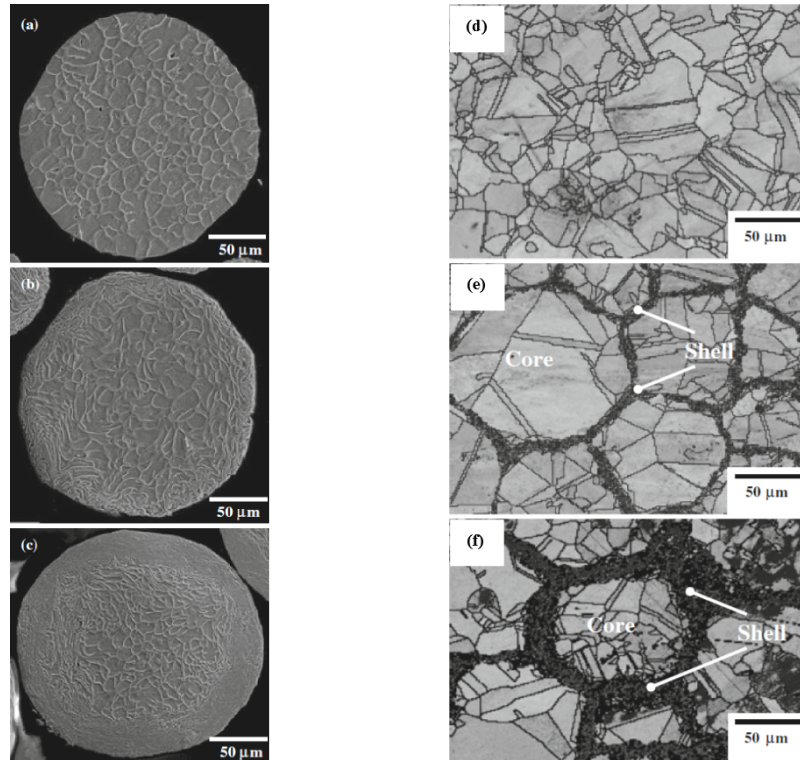


Figure 2.1 Left: SEM image displaying the cross-section of the initial powder (a), powder milled for 54ks (b) and (c) milled for 72ks. Right: EBSD image of the sintered material, displaying the core-shell areas and how its ratio alters from the initial powder (d), after 54ks of milling (e) and ultimately, after 72ks (f). Adopted from[1].

decreased resulting in a harder periphery. This shell area encompasses the central and softer undeformed region, known as the “core” area. Each particle can therefore be said to consist of a Core-Shell microstructure where the shell area increases from roughly 15 μm in the 54ks sample to around 25 μm after 72ks of MM.. Sawangrat et al. consequently concluded that the thickness of the shell area increases with an increase in milling time.

The sintered powder is displayed in Fig. 2.1d-f. Sintering the powder without milling, results in quite a homogeneous structure consisting of CG particles (Fig. 2.1d). Some darker straight lines are also evident, which is common for present procedures. However, processing the particles for 54ks (Fig. 2.1e) produces a distinct core-shell structure and this becomes even more evident after 72ks (Fig. 2.1f) of mechanical milling. The dark areas display the harder UFG shell regions with the decreased grain size encompassing the softer and brighter CG core. The microstructures morphology is highly heterogeneous on a microscale but homogeneous on a macroscale. This clear bimodal grain size distribution is therefore named the “harmonic structure”.

Furthermore, tensile tests were performed on the sintered specimens. Pure CG Cu shows fairly long uniform elongation ($\epsilon_u \sim 33.1\%$) but lacks strength as yield strength (YS ~ 94 MPa) and ultimate tensile strength (UTS ~ 205 MPa) are relatively poor. In contrary, the UFG samples display a high YS and UTS (420 MPa and 475 MPa respectively) but almost a complete absence of elongation ($\sim 3\%$). Moreover, the bimodal harmonic specimen, after 54ks of MM, shows a combination of high strength (YS ~ 109 MPa, UTS ~ 243 MPa) and long uniform elongation ($\sim 45.3\%$). The results are even clearer after 72ks of MM as can be viewed in Table 1.

To check whether the mechanical properties can be attributed to the unique morphology of harmonic structure, tensile tests were performed on a heterogeneous bimodal structure consisting of approximately 20% UFG. The results display clear advantages of the bimodal harmonic structure since elongation extends far above (roughly 53% at best) the heterogeneous sample without reducing the strength. In addition, the team concluded that

Materials	YS (MPa)	UTS (MPa)	ϵ_u (%)	Average grain size (μm), (fractions %)	
				Core/CG	Shell/UFG
Bimodal harmonic structure					
CG	94	205	33.1	32,5 (100%)	-
MM54ks + SPS (Harmonic)	109 \pm 7	243 \pm 5	45.3 \pm 7	29.2 (81%)	2.3 (19%)
MM72ks + SPS (Harmonic)	121	258	48.2	28.2 (64%)	2.0 (36%)
UFG (Cry-rolled)	420	475	3	-	0.2-0.3 (100%)
Bimodal Heterogeneous structure					
IP + MM72ks + SPS	112 \pm 15	225 \pm 17	31.6 \pm 12	31.6 (80%)	2.0 (20%)

Table 1 displaying the average mechanical properties and characteristics of pure Cu treated in the study. The harmonic structure with 19% UFG fraction and the heterogeneous structure with 20% UFG fraction are specifically compared. Since both compositions consist of $\sim 20\%$ UFG the bimodal harmonic structures mechanical performance can be attributed its unique morphology. Both CG and UFG are displayed to suite as a comparison and are not unique to this study

strength and elongation are strongly correlated with CG/UFG ratio, and the optimal ratio was found to be at 60%/40%, respectively.

2.2 Orlov et al. (2013)

Orlov et al. fabricated bimodal harmonic specimen from Cu powder with a purity of 99.96% [2]. The microstructure characteristics similar to those shown previously in Fig. 2.1 were obtained. Furthermore, tensile tests were performed using Cu with a grain size of $\sim 2.5 \mu\text{m}$ and $\sim 20.8 \mu\text{m}$ as an UFG and CG reference respectively. Both samples having the same purity as the bimodal harmonic one. The results are displayed in Fig. 2.2 as representative stress-strain curves. Typically, recrystallized CG Cu has low strength and high elongation

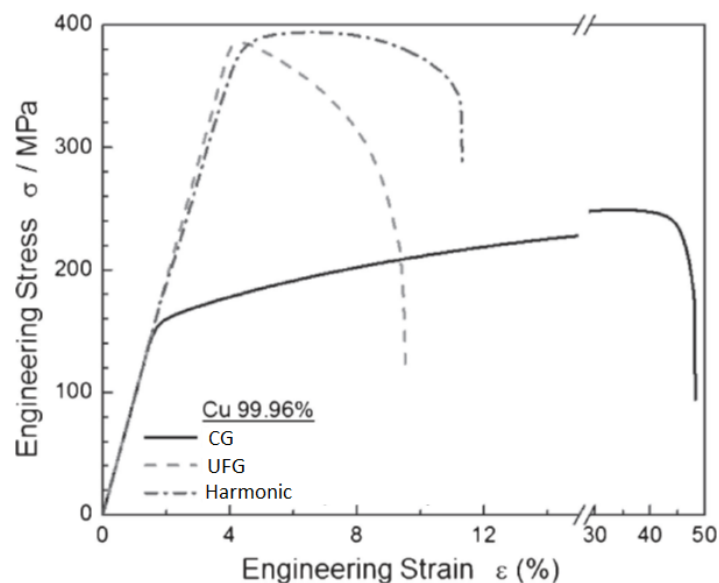


Figure 2.2 stress-strain curves for Cu with CG, UFG and a bimodal harmonic grain size structure where the latter has a combination of high strength and long elongation. Adopted from [2].

(YS ~ 156 MPa, UTS ~ 247 MPa and $\epsilon_u \sim 30\%$, respectively), and high strength but low elongation (YS ~ 360 MPa, UTS ~ 385 MPa and $\epsilon_u \sim 0.3\%$) for UFG Cu, as displayed in fig.2.2. Nevertheless, combining coarse with fine grains into a bimodal harmonic structure allows the highest strength to be obtained (UTS ~ 395 MPa). Furthermore, rather high yield strength (YS ~ 194 MPa) and an extensive improvement in elongation ($\epsilon_u \sim 2.6\%$) compared to its UFG counterpart was obtained. That kind of high strength accompanied with such an extended elongation (more than 700% improvement compared to its UFG equivalent) is quite remarkable.

2.3 Zhang et al. (2014)

Zhang along with colleagues demonstrated in this study that SUS304L steel fabricated in a bimodal harmonic structure combines a superiority of strength and ductility relative to its coarse grained and ultra-fine grained equivalents [3]. Also, the team investigated the optimal combination of CG and UFG to achieve the most advantageous material properties. This turned out to be in the samples with 41% UFG fraction where the UTS were achieved at very high 744 MPa and the YS at 382 MPa along with a high uniform elongation ($\epsilon_u = 65.6\%$). See figure 2.3. As a comparison, the UFG sample had a high strength (YS = 580 MPa, UTS = 710 MPa) but shorter elongation ($\epsilon_u = 30\%$) while the CG sample demonstrated contrariwise properties.

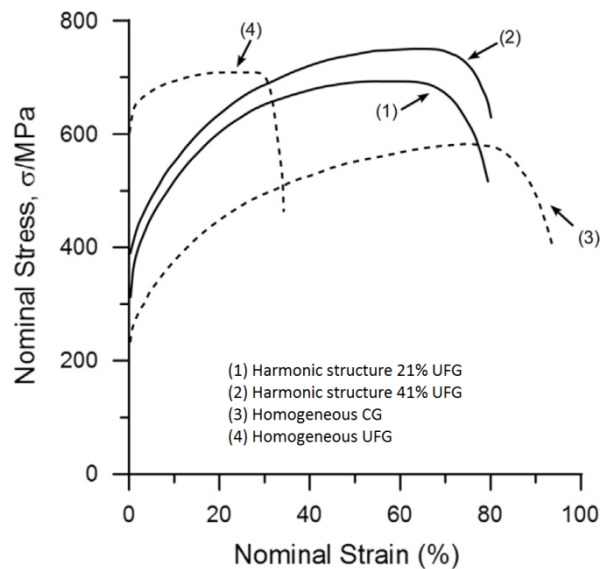


Figure 2.3 stress strain curves of SUS304L steel with different microstructure morphologies obtained by Zhang et al. in the study. Adopted from [3].

The team also examined the samples after tensile testing, using SEM, and discovered a substantial amount of cracks which were initiated in the border of the core/shell interface. Furthermore, distinct cracking arose at multiple areas around the fracture, i.e. now localized fracture.

2.4 Fujiwara et al. (2013)

Fujiwara et al. presented in this paper a composite consisting of pure titanium (core) and a Ti-Al alloy (shell) in a harmonic structured composition [4]. When the Ti-Al alloy formed 12.5 and 14.3% respectively of the total mass, the nominal stress-strain curves demonstrated most advantageous behaviour compared to the conventional Ti-Al compact. The Ti-Al alloy alone showed on average a 350 MPa as YS and 0.25% total elongation, while the harmonic composite for the 14.3% mass achieved 549 MPa and 0.34% as YS and ϵ_u respectively. An improvement by 57% in yield strength and 36% in total elongation. Further research also indicated that this composite displays good properties after high temperature treatment ($\sim 800^\circ\text{C}$) as well as after standard treatment.

2.5 Ciuca et al. (2013)

Ciuca et al. produced a harmonic structure in SUS329J1 stainless steel with significant improvements in strength ($\sim 40\%$ higher YS and $\sim 25\%$ better UTS) compared to its CG counterpart [5]. This was accompanied by a uniform elongation for 17%, which was slightly less than the bulk (CG) sample.

2.6 Ota et al. (2014)

Ota et al. fabricated homogenous (CG) and harmonic (CG + UFG) samples of pure Nickel and compared their strength and elongation after tensile testing [6]. Along with previous studies performed on other metals harmonic structured Ni also displayed an increase in strength by ($\sim 30\%$ YS and $\sim 14\%$ UTS) compared to its equivalents. The loss in uniform elongation was around 9%. The study was performed on a harmonic structure with a shell fraction of 21.4%. No optimal core/shell ratio was investigated in the study.

2.7 Yu et al. (2014)

Yu et al. performed tensile tests and a FEM analysis on harmonic structured SUS304L stainless steel and compared them [7]. The purpose of the FEM analysis was to better understand the underlying mechanism of harmonic structured materials. Even though the calculated stress-strain curve was close to the experimental one, some question marks are raised since the model was too simple to deliver a representative result at larger scale.

3 The Theory behind Stresses, Strains, Yield Criteria and the Full Newton Solution Technique realisation in Abaqus

In this chapter a brief introduction to the theory actualized during the work is presented. It is not an absolute review and shall be seen just as a guideline for the work, and a complement to subsequent chapters. This chapter describes how stresses and strains are implemented in the finite element method as well as how Abaqus does the calculations during analysis. The yield criteria for the von Mises stress has also been depicted. Subsequently, Abaqus software used for the analyses is briefly explained.

3.1 Stresses and strains

3.1.1 Stresses

Let's assume a continuous surface, onto which a force P is applied. The incremental force vector dP acts on the tiny surface dA . Normal to the surface and directed outwards is a unit vector n as well as a traction vector t [N/m^2] and can be written

$$n = \begin{bmatrix} n_x \\ n_y \end{bmatrix}; t = \begin{bmatrix} t_x \\ t_y \end{bmatrix} \quad (1)$$

The only non-zero stresses in two dimensions are σ_{xx} , σ_{yy} and σ_{xy} which results in the stress tensor S as of

$$S = \begin{bmatrix} \sigma_{xx} & \sigma_{xy} & 0 \\ \sigma_{yx} & \sigma_{yy} & 0 \\ 0 & 0 & 0 \end{bmatrix} \quad (2)$$

By referring to the reference [8] equations (1) and (2) may be written as

$$t = Sn \quad (3)$$

That in turn leads to the boundary conditions as

$$t_x = \sigma_{xx}n_x + \sigma_{xy}n_y \quad (4)$$

$$t_y = \sigma_{yx}n_x + \sigma_{yy}n_y$$

Using Gauss' divergence theorem by some minor calculations yields us the equilibrium conditions for the surface

$$\frac{\partial \sigma_{xx}}{\partial x} + \frac{\partial \sigma_{xy}}{\partial y} + f_x = 0 \quad (5)$$

$$\frac{\partial \sigma_{yx}}{\partial x} + \frac{\partial \sigma_{yy}}{\partial y} + f_y = 0$$

from which it is easy to define the matrices from

$$\tilde{\nabla}^T = \begin{bmatrix} \frac{\partial}{\partial x} & 0 & \frac{\partial}{\partial y} \\ 0 & \frac{\partial}{\partial y} & \frac{\partial}{\partial x} \end{bmatrix}; \sigma = \begin{bmatrix} \sigma_{xx} \\ \sigma_{yy} \\ \sigma_{xy} \end{bmatrix}; b = \begin{bmatrix} f_x \\ f_y \end{bmatrix} \quad (6)$$

(5) can therefore be written as

$$\tilde{\nabla}^T \sigma + f = 0 \quad (7)$$

where σ contains all the stress components, f all the forces and $\tilde{\nabla}^T$ is a matrix differential operator.

3.1.2 Strains

Prior to deformation a point in the plane is described by the coordinates (x, y) . This point has moved after deformation and has now the coordinates $(x + u_x, y + u_y)$. The changes caused by deformation are called displacement components (u_x, u_y) and are gathered in the displacement vector u defined as

$$u = \begin{bmatrix} u_x \\ u_y \end{bmatrix} \quad (8)$$

Corresponding to stresses, the only non-zero strains in two dimensions are ε_{xx} , ε_{yy} and γ_{xy} which equals to the following displacements:

$$u_x = u_x(x, y); u_y = u_y(x, y) \quad (9)$$

while

$$\varepsilon_{xx} = \frac{\partial u_x}{\partial x}; \varepsilon_{yy} = \frac{\partial u_y}{\partial y}; \gamma_{xy} = \frac{\partial u_x}{\partial y} + \frac{\partial u_y}{\partial x}. \quad (10)$$

Defining the matrix ε , that contains all the strains

$$\varepsilon = \begin{bmatrix} \varepsilon_{xx} \\ \varepsilon_{yy} \\ \gamma_{xy} \end{bmatrix} \quad (11)$$

makes it possible to write the kinematic relations (10) as

$$\varepsilon = \tilde{\nabla} u \quad (12)$$

Where $\tilde{\nabla}$ equals the matrix used for stresses and is defined by (6).

3.2 Yield criteria

To determine when a material goes from elastic to plastic behaviour can be done using at least two main approaches. The most common, and the one used in the present dissertation, is the von Mises criterion. Plasticity is initiated when the yield stress (σ_s) is reached. In two dimensions the von Mises yield stress criterion can be illustrated by an ellipse in the $\sigma_1\sigma_2$ -

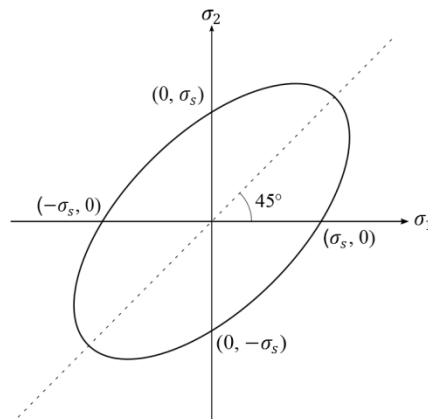


Figure 3.1 von Mises ellipse in the $\sigma_1\sigma_2$ -plane.

plane. See fig. 3.1. Taking advantage of a reference [9] once more, the yield criterion can be written as

$$\sigma_{e,Mises} - \sigma_s = 0. \quad (13)$$

Meaning that when the von Mises stress $\sigma_{e,Mises} < \sigma_s$ the response is said to be elastic, if $\sigma_{e,Mises} = \sigma_s$ plasticity is initiated and when $\sigma_{e,Mises} > \sigma_s$ resulting in plasticity of the material. Where von Mises stress is defined by

$$\sigma_{e,Mises} = \sqrt{\sigma_1^2 + \sigma_2^2 - \sigma_1\sigma_2}. \quad (14)$$

3.3 Full Newton solution technique

The generated finite elements in Abaqus can involve from a few to thousands of variables in a commonly nonlinear model [10]. The equilibrium equation can generally be written as

$$F^N(u^M) = 0 \quad (15)$$

This equation is to be solved throughout the time step of interest where F^N contains the force components coupled with the N^{th} variable in the problem and where u^M corresponds to the value of the M^{th} variable. Each time step is divided into many increments that are unique both in size and number for each solution. Two main issues emerge: how to solve the discrete equilibrium equation (15) and how large increment size should be chosen at each increment. If we make the assumption

$$F^N(u_i^M + c_{i+1}^M) = 0 \quad (16)$$

where after an iteration, i , the approximation u_i^M to the solution has been acquired. Furthermore, c_{i+1}^M is the difference between the exact solution and this solution. If the assumption is further expanded in a Taylor series this is the result

$$F^N(u_i^M) + \frac{\partial F^N}{\partial u^P}(u_i^M)c_{i+1}^P + \frac{\partial^2 F^N}{\partial u^P \partial u^Q}(u_i^M)c_{i+1}^P c_{i+1}^Q + \dots = 0. \quad (17)$$

The difference, c_{i+1}^M , will be small when the approximation u_i^M to the solution is close. Therefore, the last terms can be neglected resulting in a linear system of equations:

$$K_i^{NP} c_{i+1}^P = -F_i^N \quad (18)$$

Where the Jacobian matrix is as follows

$$K_i^{NP} = \frac{\partial F^N}{\partial u^P}(u_i^M) \quad (19)$$

while the force equation for increment i might be written as

$$F_i^N = F^N(u_i^M). \quad (20)$$

Abaqus will then make, for the next increment, the approximation to the solution by

$$u_{i+1}^M = u_i^M + c_{i+1}^M \quad (21)$$

and the iteration continues until the entire system is solved, or if no solution is to be found, terminate the process. Abaqus will do so if no solution has been found after five consecutive increments.

3.4 Brief Introduction to Abaqus

Abaqus FEA is a software in the SIMULIA brand developed by Dassault Systems Inc. for computer-aided engineering and finite element analysis. It is widely used in the aerospace and automotive industry, as well as in the academia and is applied for solving both routine and highly advanced engineering problems. Abaqus uses the open-source scripting language Python where input-files for the solver can be created either in the visualization mode or by using a common text editor. The program suite primary consists of five products which of two will be explained more closely.

1. Abaqus/CAE
2. Abaqus/Standard

Using **Abaqus/CAE** (Complete Abaqus Environment), a visualization mode, one can create or import geometry, edit, define material properties, creating a mesh, monitoring and visualize both pre- and post-processing, utilizing the many modules that Abaqus/CAE is divided into. The working environment is simple and logical when learned but at the same time highly

complex where users follow several steps when going from module to module creating the model, as will be explained in sections 4.1 to 4.4 . Finally, the results are viewed.

Abaqus/Standard is one of two solvers in the program suite with a solution technology optimized for static and low speed dynamic events (Systems, u.d.). The solver reads the input file, processes it, before eventually generating an output database. In the present dissertation Abaqus/Standard will be the main choice due to the static response of the model.

4 Finite Element Analysis of Harmonic and Heterogeneous Structures in Abaqus

In this chapter an extensive description of the FE-analysis of harmonic and heterogeneous structures will be described. Most of the time has been spent on developing the model of harmonic structure since this was the main goal of the dissertation. This consists of two variants, one for coarse mesh and one for finer. The model of heterogeneous structure was used for comparison with harmonic structured one. If not mentioned otherwise, Abaqus interface is the main working directory. The input file can be found in appendix.

4.1 Model Development

The basic geometry of the model is very simple, consisting of a square measuring 1×1 [mm] with a circle in the centre, see fig 4.1a. The circle represents the CG area (green in figure) and should thus correspond to 60% of the total area leading to a radius of $r = h \sqrt{\frac{3}{5\pi}}$ [mm]. The area inside the square, but exterior to the circle (light grey in figure), represents the UFG region and constitutes the first 40% of the model. For the coarse mesh, this geometry is sufficient, but in order to acquire a sufficiently fine mesh in the areas of interest some geometrical features were added as shown in fig. 4.1b. The added lines are simply partitions

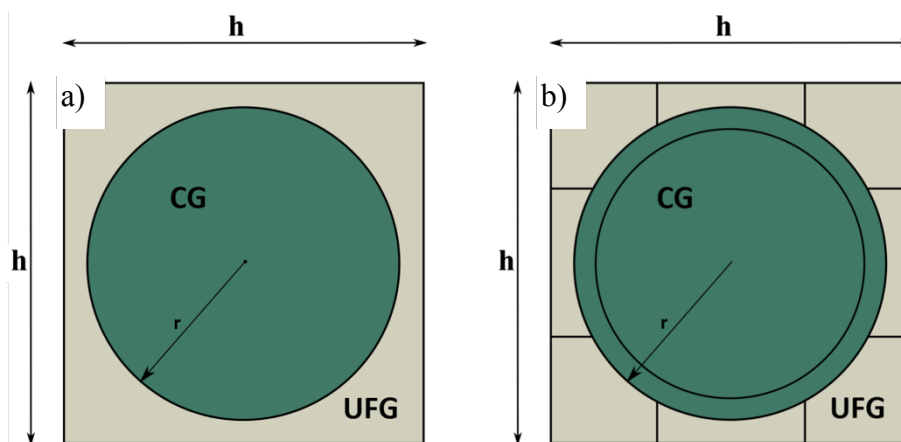


Figure 4.1 basic geometry (representative volume element) of the model when coarse (a) and (b) fine meshes are used during the analyses.

in the geometry and purely exist to control the concentration of mesh in some areas. This will be explained in details in chapter 4.4. Many different varieties on the partition for the fine mesh geometry were tested but this was found to be the most efficient due to its simplicity and the resulting meshes. In fact, the simplicity was a major factor to consider when creating the geometry. A more complex model might have the potential to deliver more accurate results but there is also a higher risk of failure. In the present work the simple models had both the advantage of being precise as well as non-problematic.

The basic geometric units were assembled into a full-scale geometry containing 500 units and with the total dimensions of 10x50 [mm], as can be viewed in fig. 4.2. These dimensions were chosen after careful consideration of how to mimic a bimodal harmonic structure in the best and most simple way possible while maintaining a great resolution in both x- and y-direction in the analysis. For the fine mesh geometry (fig. 2b) the intersecting horizontal and vertical lines were removed while the same lines were left alone for the coarse mesh (fig. 2a). This was a result of trial and error based on the experience of elaborating an acceptable mesh.

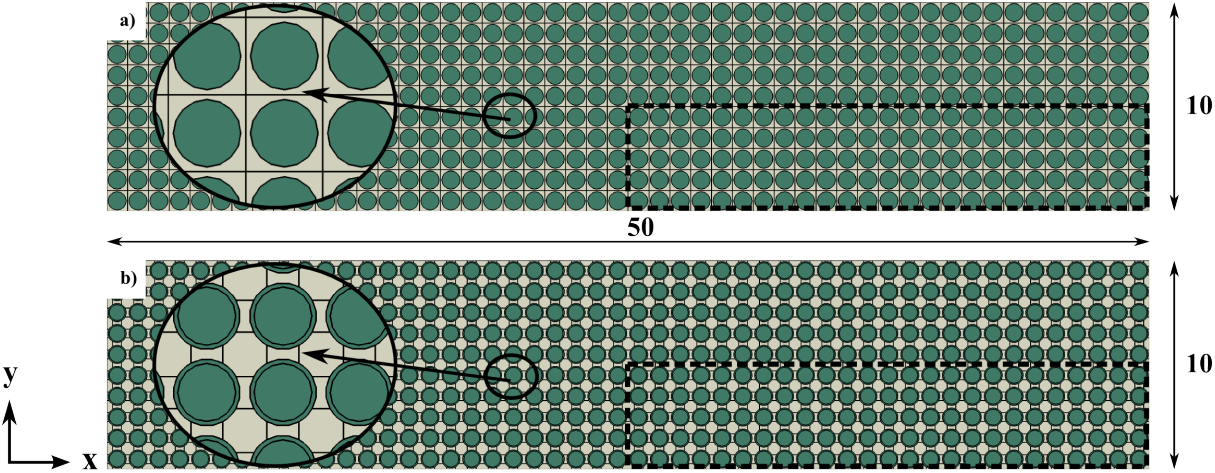


Figure 4.2 fully assembled geometry of (a) coarse and (b) fine mesh consisting of 500 units each. Both consist of 50 basic units in x-direction and 10 in y-direction to obtain a sufficient resolution in the analysis.

4.2 Boundary and Initial Conditions

Due to the symmetry of full-scale geometry, the analysis was performed on one quarter of a real sample by applying symmetric boundary conditions (BC) along the top (y-sym.) and left (x-sym.) dotted lines, as can be viewed on the right part of fig. 4.2. This made it possible to significantly reduce the computational time. Figure 4.3 displays the final model of simulations of coarse (fig. 4.3a) and (fig. 4.3b) fine mesh geometries. On the right-hand side of the model, displacement BC was applied leaving the model free to move in y-direction while assigning a specified displacement in x- direction for each analysis. No rotation was allowed.

A static, general step was utilized, using automatic incrementation, allowing Abaqus/Standard to modify the value throughout the step with a small minimum size ($1e^{-10}$). Abaqus solver will terminate the analysis if a smaller size is needed to solve the equation [12]. Maximum size and maximum number of increments are decreased and increased respectively preventing the solver from approaching critical areas too rapidly, and from aborting due to too few increments. None of those settings can be said to be general but are rather specific for each model. *Nlgeom* was also activated to control the nonlinear effects of large displacements while the *Full Newton* solution technique was implemented in general.

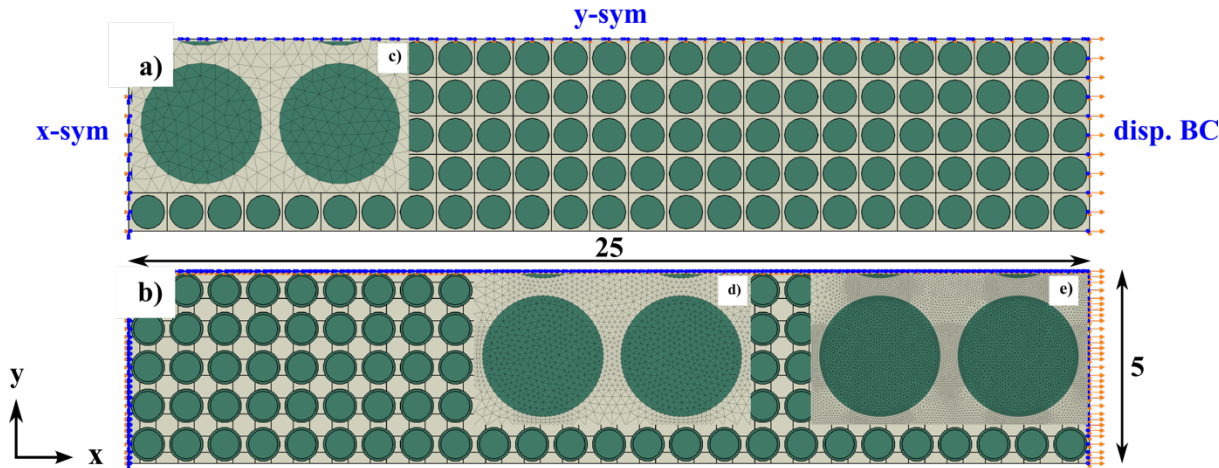


Figure 4.3 final model equipped with symmetry and displacement BC for (a) coarse mesh and (b) fine mesh. Due to its symmetry the computational time was shrunk to roughly one quarter. (c) shows the meshed model represented by one third coarse, medium fine (d) and fine (e) mesh respectively. Note that model (a) is used for the coarse mesh (c), while model (b) is used for the medium (d) and fine (e) meshes.

4.3 Material data

Mass density, ρ was set to 8890 kg/m^3 while the elasticity was defined by Young’s modulus and Poisson’s ratio, ν to 210 GPa and 0.31 respectively. It is worth to point out that these data are equal for both CG and UFG. For the description of material rheology, raw experimental Nickel CG data for stresses and strains were extracted from in-house tensile tests. The dimensions of specimens were $5 \times 1.31 \text{ [mm]}$. Cropping at UTS and $\sigma_{0.2}$ to remove excessive data was done next. Furthermore, since the experimental outputs were not increasingly monotonic, interpolation was required for Abaqus to use it. This was done in MATLAB MathWorks operating “*polyval*” and “*polyfit*” inbuilt functions. A 19th degree equation was found to be optimal. Engineering stress-strain data were converted to true stress-strain data using equations 22

$$\sigma_T = \sigma_E(1 + \epsilon_E) \tag{22}$$

and 23 [13]

$$\epsilon_T = \ln(1 + \epsilon_E) \tag{23}$$

respectively. See appendix B for the MATLAB code for this. YS and UTS for CG were read from the interpolation and equals to 160 MPa and 596 MPa respectively.

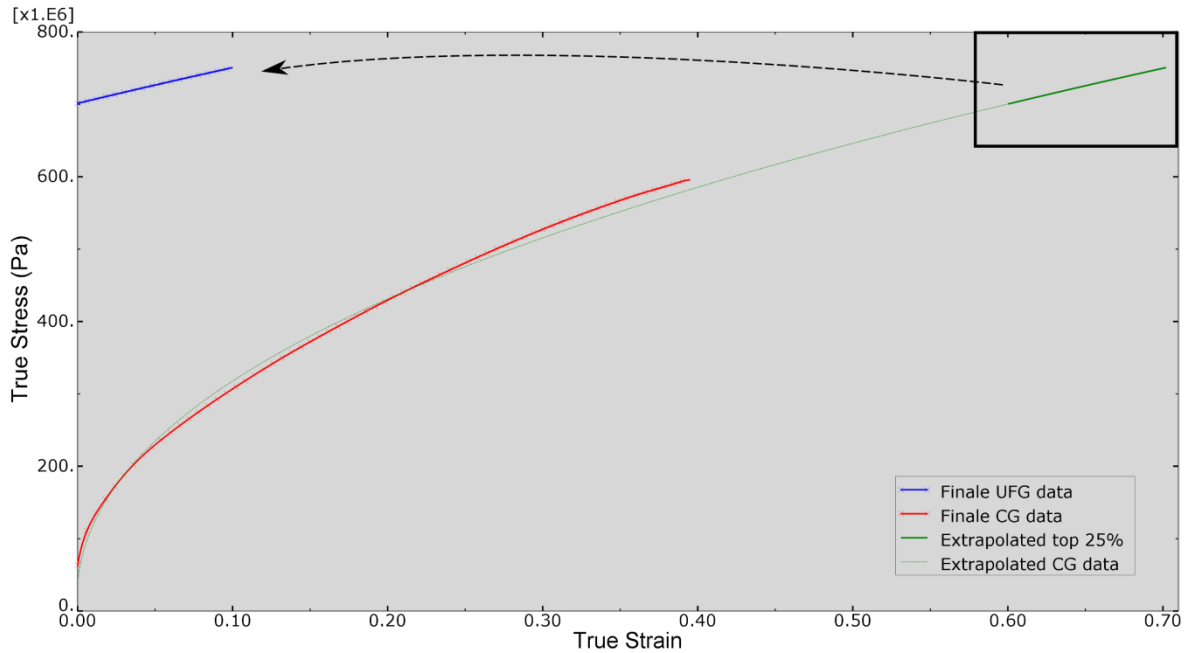


Figure 4.4 CG (red) and UFG (blue) data used as plasticity input in Abaqus/CAE as well as visualizing the method used for extracting UFG from CG data (green).

No reliable UFG data was found due to the difficulties to perform such tensile tests. Instead, the CG data was extrapolated up to roughly 750MPa, extracting the UFG data from the top, corresponding to 25% of the CG elongation. YS and UTS for UFG input data equals 712MPa and 751 MPa respectively. The procedure is demonstrated in figure 4.4. The red curve displays the final CG data and the blue one the final UFG data utilized as plasticity input in Abaqus/CAE.

It is interesting to note the differences between the CG and UFG data meaning that an elongation of 10% equals roughly 307 MPa in true stress for the coarse grained data while the same elongation corresponds to 751 MPa for UFG.

4.4 Mesh Development

The development of a mesh suitable for the large deformations in the body took significant time. These problems were largest when the amount of elements was highest i.e. the elements were smaller. A larger element was found to be able to withstand a larger amount of elongation before it failed (non-relative to its size) compared to its smaller counterpart. This had to be weighed against the resolution wanted. Plane strain, 3-node, linear element (CPS3) type was used with default settings. Distortion control was not possible to combine in two dimensional elements in Abaqus, but the triangular shape was chosen owing to their advantage of coping with deformations better than other element shapes, as well as to minimize mesh errors at the circle borders.

4.4.1 Coarse Mesh (28k Elements)

The coarse mesh model totally constitutes of 28 310 elements with an approximate element size of 0.1 and curvature control 0.05. These settings were found to generate good results. Moreover, the computational time was very short. The meshed model in addition to a magnification can be viewed in fig 4.3c.

4.4.2 Medium Fine Mesh (150k Elements)

Medium fine mesh embodies 149 524 elements, roughly five times more than the coarse, and with four elements in between the CG areas in x- and y-direction. Aiming for a higher resolution this mesh was set up with a general approximated element size of 0.1 with 0.015 curvature control. In areas where a finer mesh was of interest, partitions were made, as demonstrated in fig 4.1b. This had to be done to control the mesh in critical areas in a desirable way [14]. The partitions were optimized during the simulations. The finer meshed zones had an approximate element size of 0.04 and curvature control 0.01. See figure 4.3d.

4.4.3 Fine Mesh (720k Elements)

The fine mesh consists of 720 930 elements with ten elements between the CG zones in x- and y-direction allowing more accurate results. 0.05 and 0.009 were used for the element size and curvature control adding 0.007 for the latter in the central round areas of the CG region. Between the circles in the high refined sections 0.015 and 0.006 respectively was defined. Figure 4.3e demonstrates the result.

4.5 Heterogeneous structure

As explained in the introduction section, a part of this projects aim was to compare a harmonic structured material to its heterogeneous counterpart. Subsequently, a random distributed composition had to be developed. It shall be noticed that less time was devoted for this part with strict approximations as a result. Figure 4.5 demonstrates schematically what the heterogeneous model constitutes of and its proportions. This model had, apart from some minor changes described below, similar fraction of UFG as the harmonic structure.

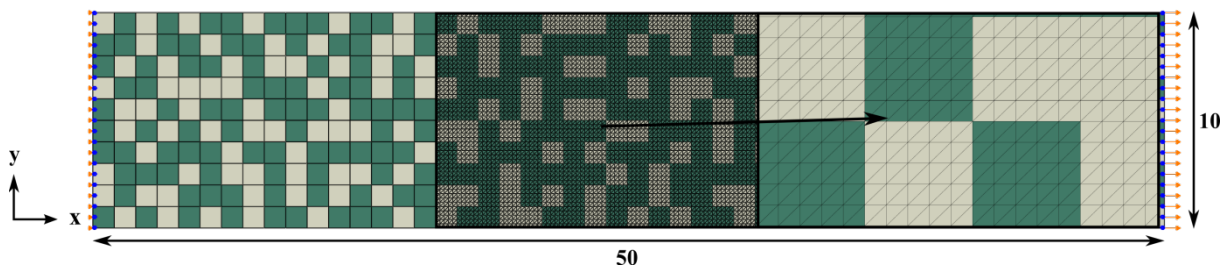


Figure 4.5 heterogeneous structure with boundary conditions. The central and right part of the figure exposes the mesh used for the model as well as a magnification of the same. UFG are shown as light grey zones.

4.5.1 Model Development

The heterogeneous model was created from simple squares, as displayed in fig. 4.1a. This was in turn assembled, consisting of 500 squares, into the total dimension of 50x10 [mm], shown in the left part of fig. 4.5.

4.5.2 Boundary and Initial Conditions

No symmetry was applied since this would partly counteract the random distribution. Both the models left and right side (fig. 4.5), no constraints were added in y-direction while revolution was impeded. In x-direction the left side was fixed leaving the right side free to apply the deformation. The areas with UFG and CG were randomly distributed with the same relationship (40% and 60% respectively) as in the harmonic structure. Green zones represent CG and light grey UFG.

4.5.3 Mesh Development

The random distributed model was meshed with 25 000 elements of the same kind as was used for the harmonic structure. To enable a better comparison, the number of elements were selected as close to the coarse meshed harmonic structure as possible. Choosing slightly lower number of elements was opted due to the fact that fewer elements yields in general less accurate results. This made it possible to pull the sample further, similar to the HS specimen. The approximate element size was set to 0.2 and no curvature control.

5 Results and Discussions

The coarse, medium fine and fine meshed models will be presented simultaneously to simplify the comparison between them for the reader. All figures display one quarter of the total model, just as visualized in fig. 4.2.

5.1 Verifying the Models

Before any results can be trusted the models needed to be verified. This was achieved by assigning both the CG and UFG sections with the same material properties and perform a number of analysis, meaning that the entire model contained either exclusively coarse or fine grains. This was done for both the coarse and fine mesh model (fig. 4.3) as well as for the heterogeneous one (fig. 4.6). Referring to these means that the whole model was either entirely green (CG) or completely light grey (UFG). Figure 5.1 evince the verification for the coarse and fine meshed as well as for the heterogeneous model. All three models follow the reference, or tabular data, very well in terms of both the CG and UFG. The discrepancy between the coarse mesh and fine mesh model is roughly $6 * 10^{-5}$, meaning far less than 1%,

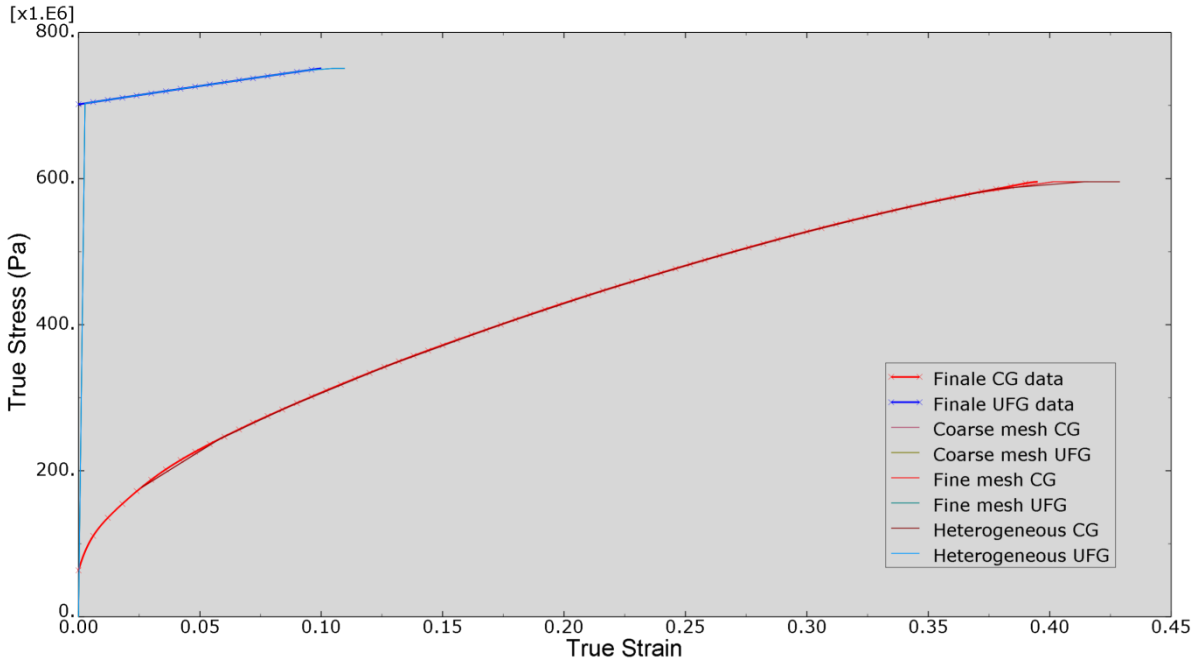


Figure 5.1 verification of the harmonic coarse and fine mesh models as well as the heterogeneous one. It is easy to see that all three models correspond well both when the analysis is performed using uniformly CG and UFG.

and can therefore be considered as acceptable. The deviation for the heterogeneous model is roughly the same.

To prevent confusion, the first dot (0, 0) in the stress-strain data plot for all three specimens were neglected and removed, regarding the CG data, leaving the first dot to be at YS (160 MPa). When true strain has reached roughly 0.4 and 0.1 for CG and UFG respectively all the models form a straight horizontal line indicating constant value of stress level. This reaction is due to the input provided to Abaqus. In the figure all the models have been pulled just past the last point of data. With these results, the model can be considered as valid and should therefore be used also with bimodal material distribution i.e. bimodal harmonic structure.

5.2 von Mises stress distribution at large scale

Figure 5.2 demonstrates the results for von Mises stresses for 28k, 150k and 720k elements. To facilitate comparison, the limits have been set to be equal to the 28k analysis. Likewise, the samples have been pulled the same distance (8%), which equals roughly to the very fine mesh's maximum.

The uniform distribution at large scale is obvious, which is very representative for harmonic structured materials. This is one of the critical reasons why harmonic structures have demonstrated superior properties compared to its CG and UFG counterparts, as described in chapter 2. Tensile strain is distributed over a larger domain rather than accumulate in critical areas, which enables large total deformations. The highest stresses emerge in the shell section, exterior to the circles, and reach their peak in the areas where the UFG zones are as most narrow. This occurs in x- and y-directions where the CG spheres are closest to each other with an absolute peak in the latter.

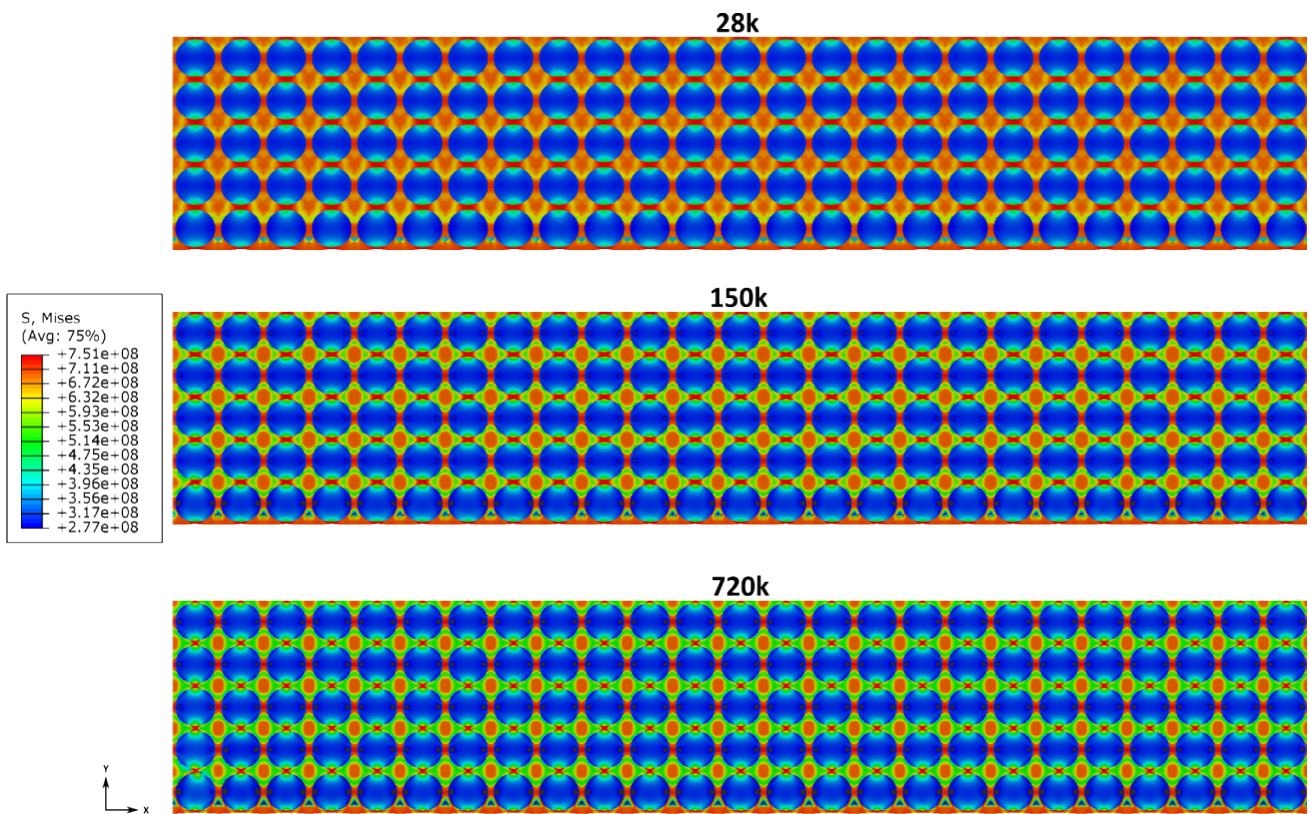


Figure 5.2 von Mises stress distribution for 28k, 150k and 720k elements.

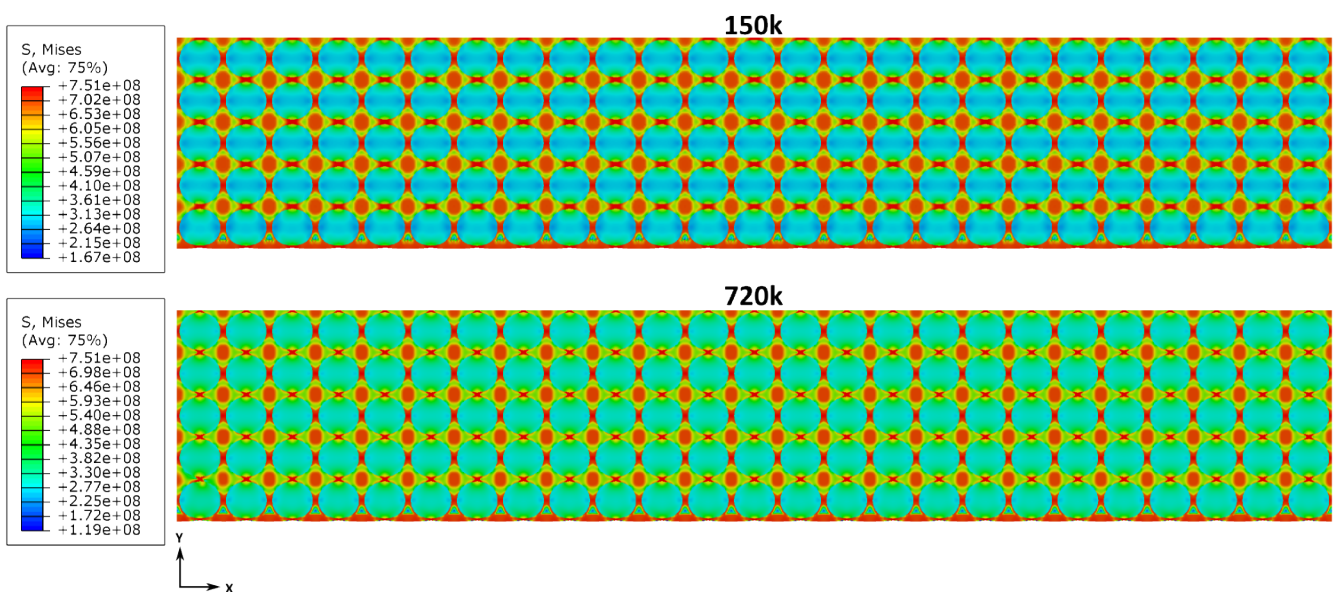


Figure 5.3 von Mises stress distribution for the 150k and 720k meshed models with pre-set limits, meaning that the legend differs. Except that, this figure shows exactly the same as in corresponding fig. 5.2. 28k mesh is not displayed since it would be equal to what can be viewed in fig. 5.2.

Figure 5.2 also works as a verification of the model, given the very uniform results when different meshes are compared, except the higher resolution obtained with the finer mesh (150k and 720k). This larger resolution displays the distribution of stresses as less scattered across the shell (compared to 28k), but rather as concentrated to a few zones, marked bright red in the figure. The likelihood of material failure is largest in these areas.

The very top side of the models (i.e. the central part of the total geometry) demonstrates slightly lower stress dispersion than the bottom with higher and more uniform stress distribution. There is rather clear difference between the coarse and finer meshed analysis. The divergence between fine and very fine meshes are slim. Figure 5.3 displays the same results with automated legend resulting in a complete different colour distribution. This also enables all areas to be coloured in the finer meshed samples which isn't the case in fig. 5.2.

5.3 Equivalent plastic strain distribution at large scale

The results for the equivalent plastic strain distribution are displayed in figure 5.4 and 5.5. Note that the limits have been set similarly as they were for the von Mises stress distribution. A uniform pattern is seen across the entire model, with just slight variations between different meshes. Opposite to what was present for the stresses, the strains are mostly concentrated in the softer CG spheres while the UFG area almost is exempt for displacement, except for some critical areas. The equivalent plastic strain reaches its maximum in the same zones as the von Mises stress. In figure 5.5, it is clear where the strain locally reaches those limits (green/yellow-red areas) and uniformly distributes mainly into the core region. With the finer mesh, these zones are even slimmer resulting in extensively larger strains.

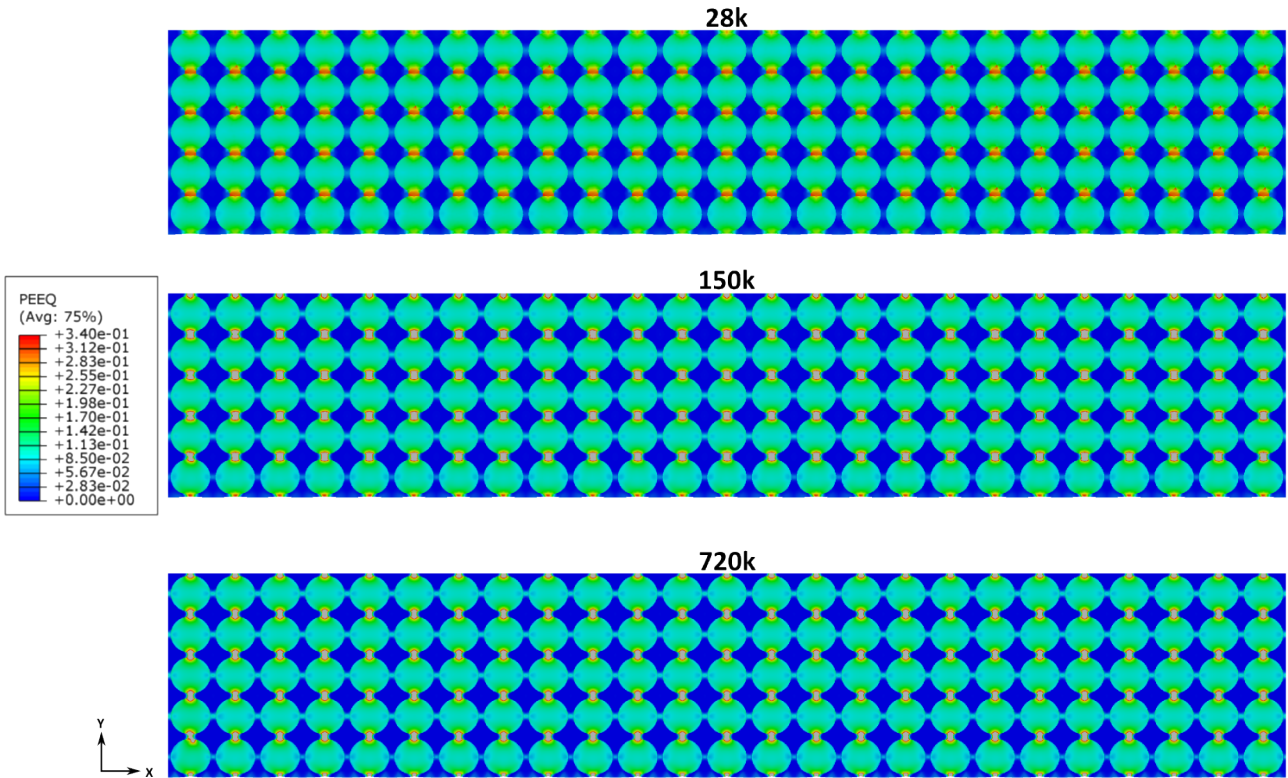


Figure 5.4 equivalent plastic strain with equally calibrated limits for 28k, 150k and 720k number of elements. Typically for harmonic structured materials a homogeneous pattern is present distributing the strains over a larger area.

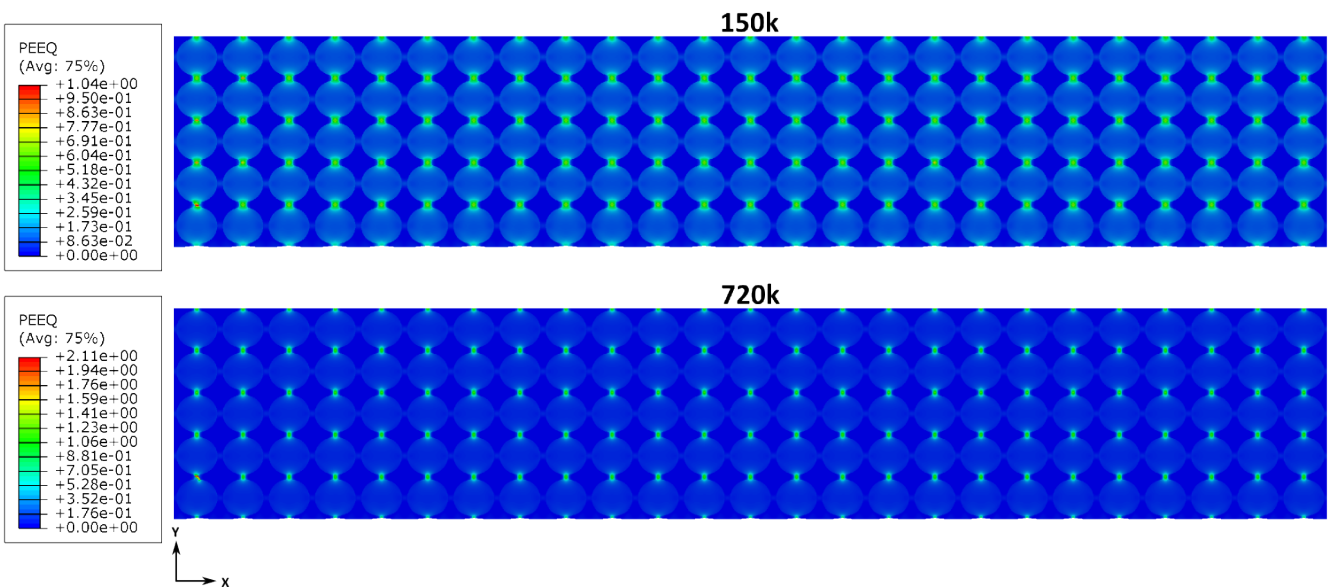


Figure 5.5. Equivalent plastic strain for 150k and 720k number of elements displaying the entire colour spectrum. Other than that, it equals to fig. 5.4.

5.4 Stress and strain distribution at close

While stress and strain distributions at large scale is allocated in a rather consistent pattern across the entire model there are significant differences at a closer look. Figure 5.6 demonstrates this. Note that the scales have been set to match the coarse 28k mesh (pic. a, b) while there are some areas in grey for the finer mesh (pic. c, d, e and f). These grey areas are due to the finer meshes capability to deliver a more accurate result. In the lower edges of each picture an interesting wave like shape is present. The model deforms more in the cross-section under the circular softer CG areas than it does in the harder UFG intersection.

It is more evident that the stresses (a, c, e) are mainly distributed in the harder UFG zones with maxima occurring in-between the cores. From here on the decline happens rather rapidly into the enclosed areas with a large difference in stress altitude entering the core. This immediately difference is slightly smaller with higher resolution (c, e). The strains (b, d, f) on the other hand, are mainly located in the core as mentioned previously with maximal strains in the same area as the highest strains.

From a closer perspective, it is more evident how large the restrictions are for the coarse meshed model. In fig. 5.6b the coarse mesh delivers a very poor result. On the other hand, there are minute visual differences between the finer meshed models that in turn might make the 150k model well suited for future work when both accuracy and computational time is considered. The models have been pulled the same distance in figure 5.6 and 5.7 without any fracture when coarse mesh is applied.

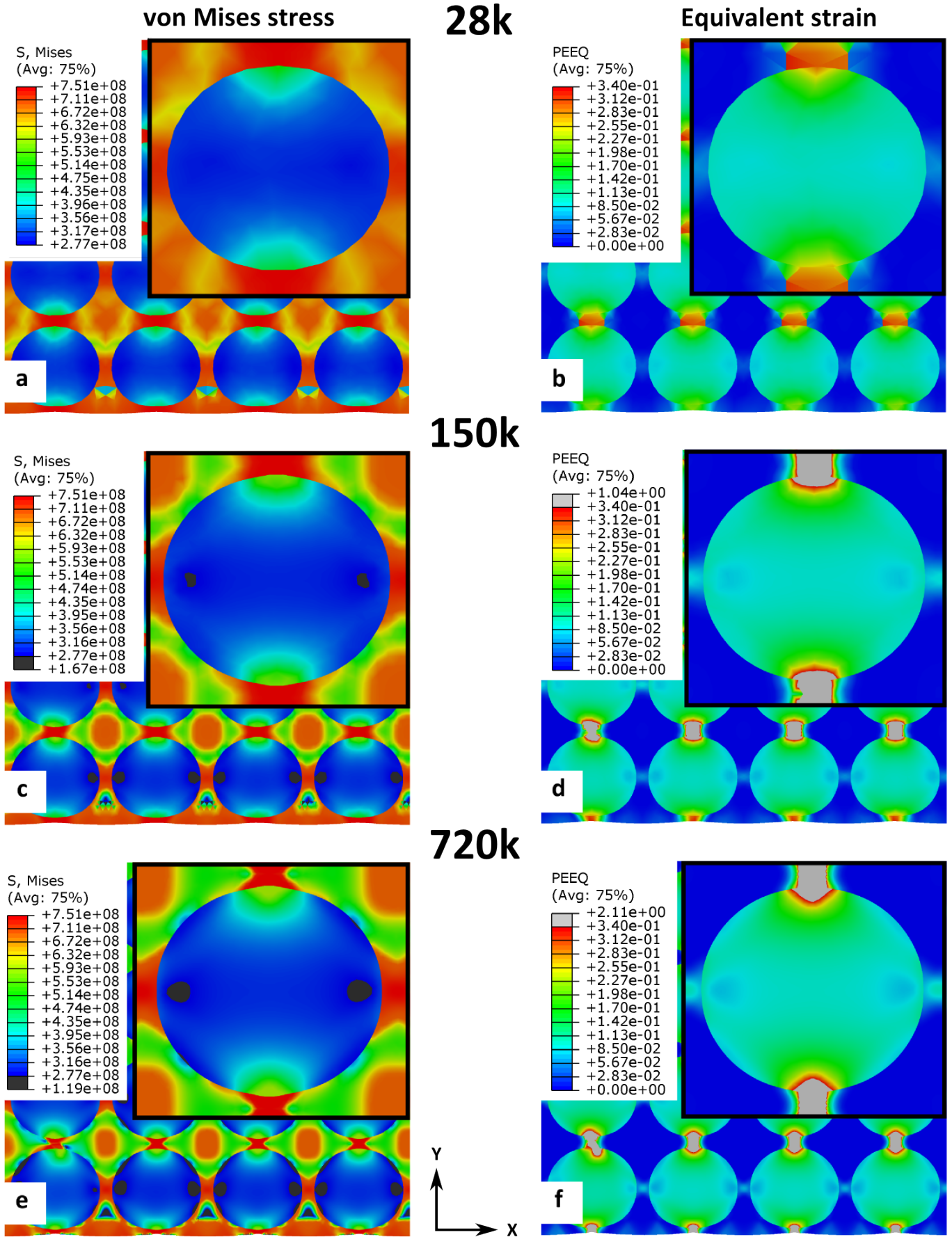


Figure 5.6 von Mises stresses (a, c, e) and equivalent strains (b, d, f) for coarse (28k) and fine meshed (150k and 720k) alternatives. The legend has been set to match the coarse meshed model.

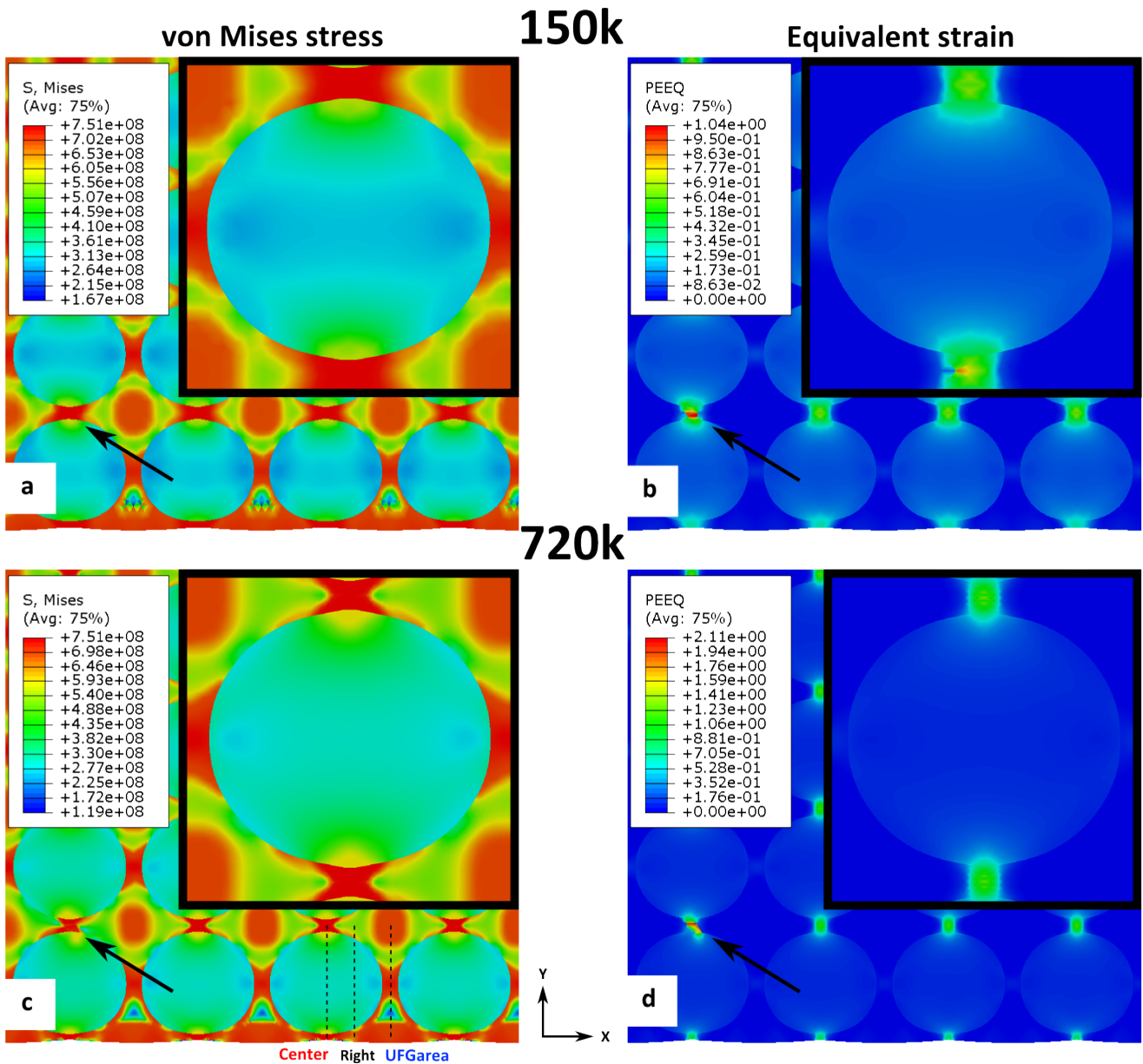


Figure 5.7 von Mises stresses (a, c) and equivalent strains (b, d) for the finer meshed models with a complete colour spectra. Also, a critical area with severe element deformation can be noticed (arrow).

However, in the area marked (fig. 5.7), there is larger deformation. This might be due to the high magnification following the finer mesh, resulting in the beginning of fracture in the material. This is a most probable explanation. An alternative explanation can be in the fact that severe element deformation accumulated with a mesh that locally cannot produce a reliable result. A re-mesh in such zones would most likely solve the problem. The reason for this happening with finer mesh might be due to the regional deformation is far more extensive relative to the small elements. The small elements cannot simply cope with the deformations. Note that it is the relation between the element size and the local deformation magnitude that

might be critical. This will be further demonstrated in chapter 5.6. These arguments most likely explain the majority of differences in maximal strain (34%, 104% and 211% respectively) for the three variants of mesh density (see fig. 5.6b, d and f as well as fig. 5.7b and d). The areas situated above the wave pattern but between the lower cores, not marked (fig. 5.6a, c and fig. 5.7a). This inaccuracy is mostly due to insufficient meshing and is solved in the highest resolution simulations (fig. 5.6e and fig. 5.7c).

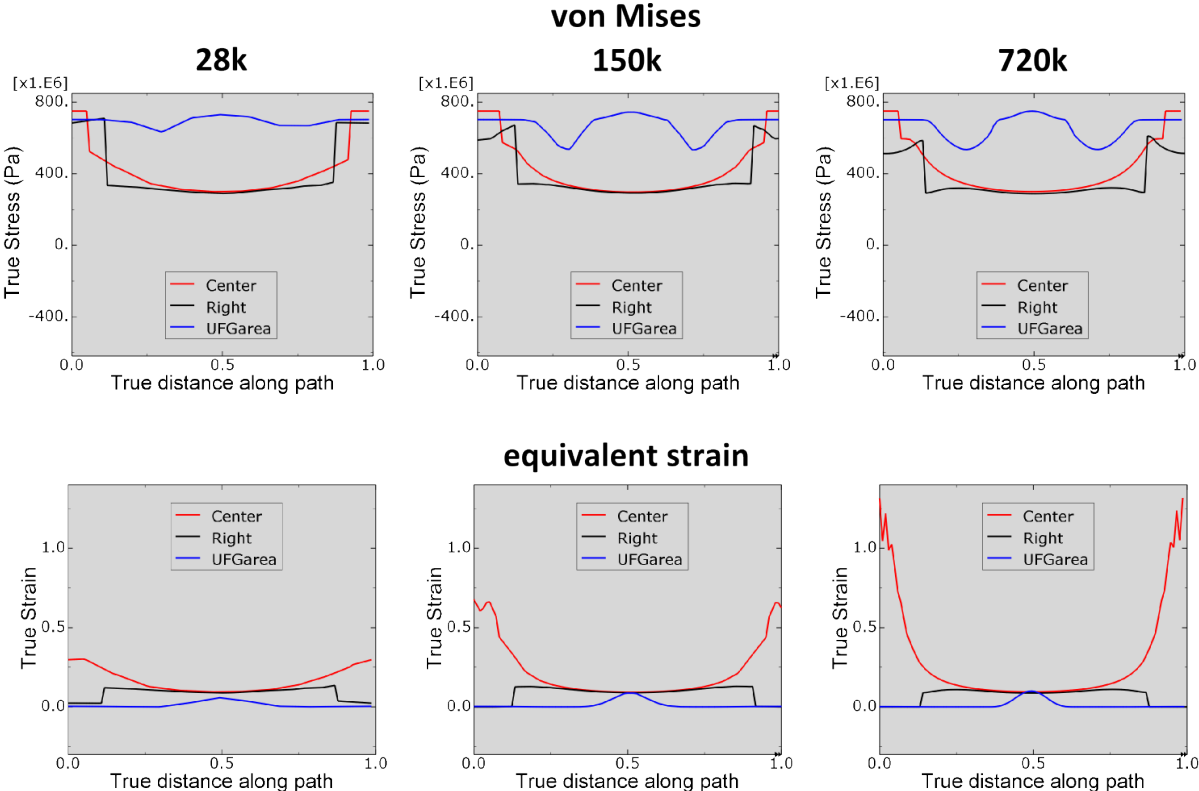


Figure 5.8 the von Mises stress and equivalent strain along the paths displayed in fig. 5.7c.

5.5 Stresses and strains in x, y and xy directions

Stresses (a, b, c) and strains (d, e, f) are presented in figure 5.9, 5.11 and 5.13 visualizing the bottom left area of the model (where the arrow is pointing in figure 5.7). Corresponding plots displaying the stress and strain components along three paths (“Center”, “Right” and “UFGarea”) can be viewed in figure 5.10, 5.12 and 5.14. As could be expected, the highest values are located in x-direction (a, d) for both the strains and stresses since the sample is pulled that way. Interestingly, rather large negative stresses, i.e. compression, arise in the UFG zones between the cores (see (b) in fig. 5.9, 5.11 and 5.13 with matching plots).

There are also areas where a substantial negative stress is evident resulting in localized compression (b, e). Moreover, it can be viewed, for all three mesh alternatives in (c) that shear stress is present in the circular border of CG and UFG. The stress applied to the model pulls the core and shell areas apart following a stress distribution in the area. This shear stress is very likely the reason for the cracking to initiate in the fringe as Zhang et al. observed and is mentioned in chapter 2.3. As that team discovered the cracks arose at multiple areas rather than in a few localized zones. This model confirms those observations very well. In (f) the outcome from the shear stress can be viewed resulting in the opposite acting strains where one side of the CG area is stretched while the other is compressed.

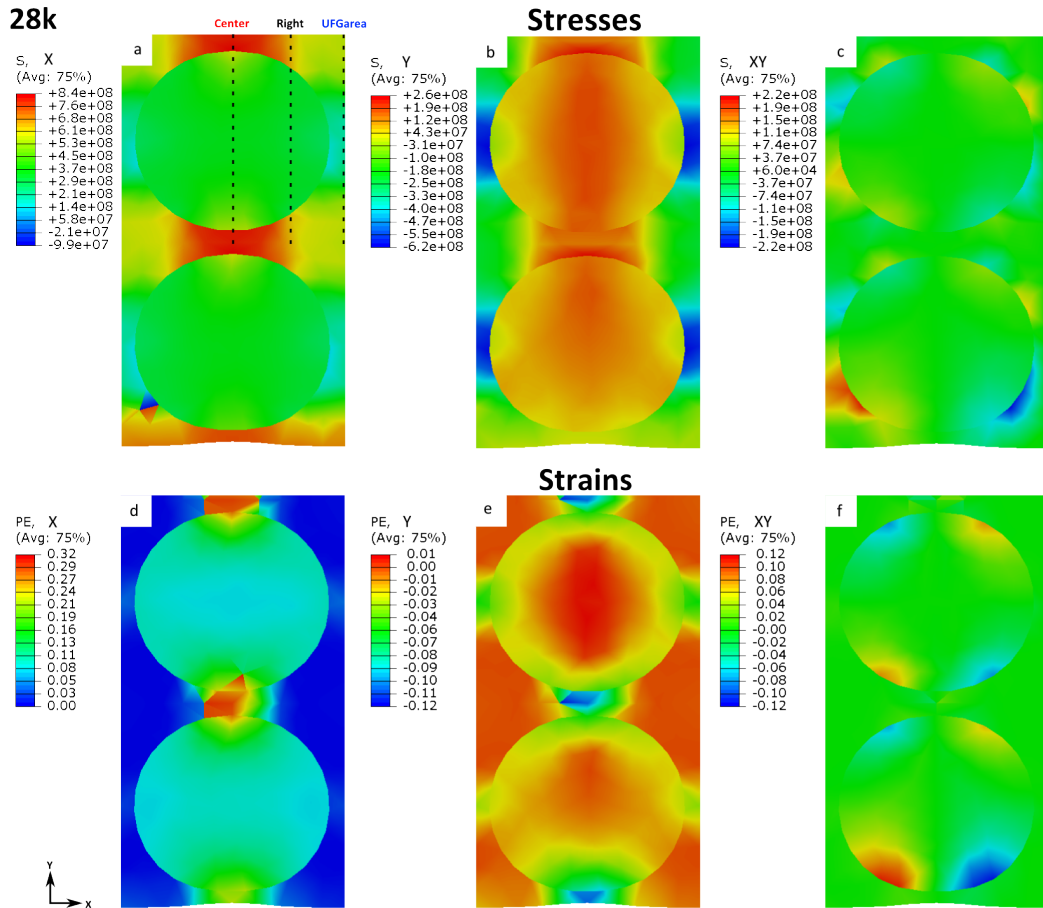


Figure 5.9 stresses and strains for coarse mesh in x , y and xy direction. Note the shear stresses in (c) that results in cracking mentioned in Ch. 2.3.

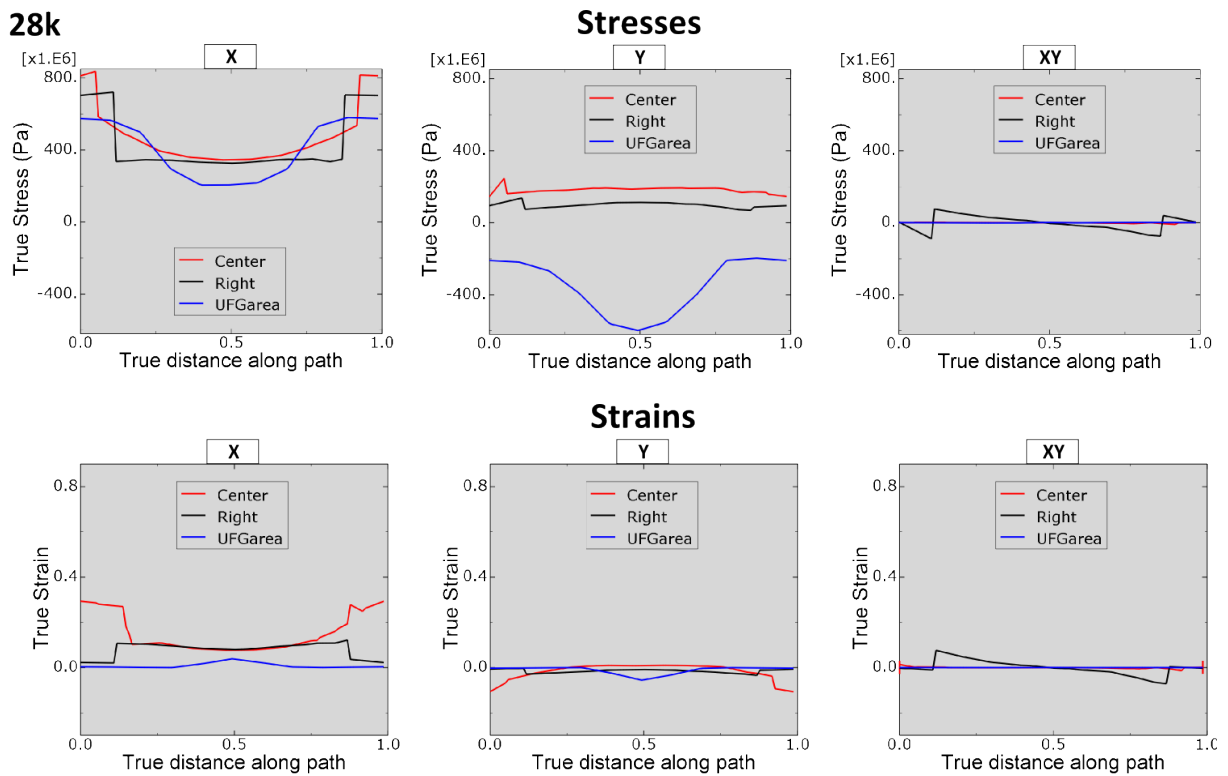


Figure 5.10 stress and strain components for coarse mesh in x , y and xy -direction, corresponding to the imagery shown in fig. 5.9a. The components are plotted along the paths visualized in fig. 5.9a.

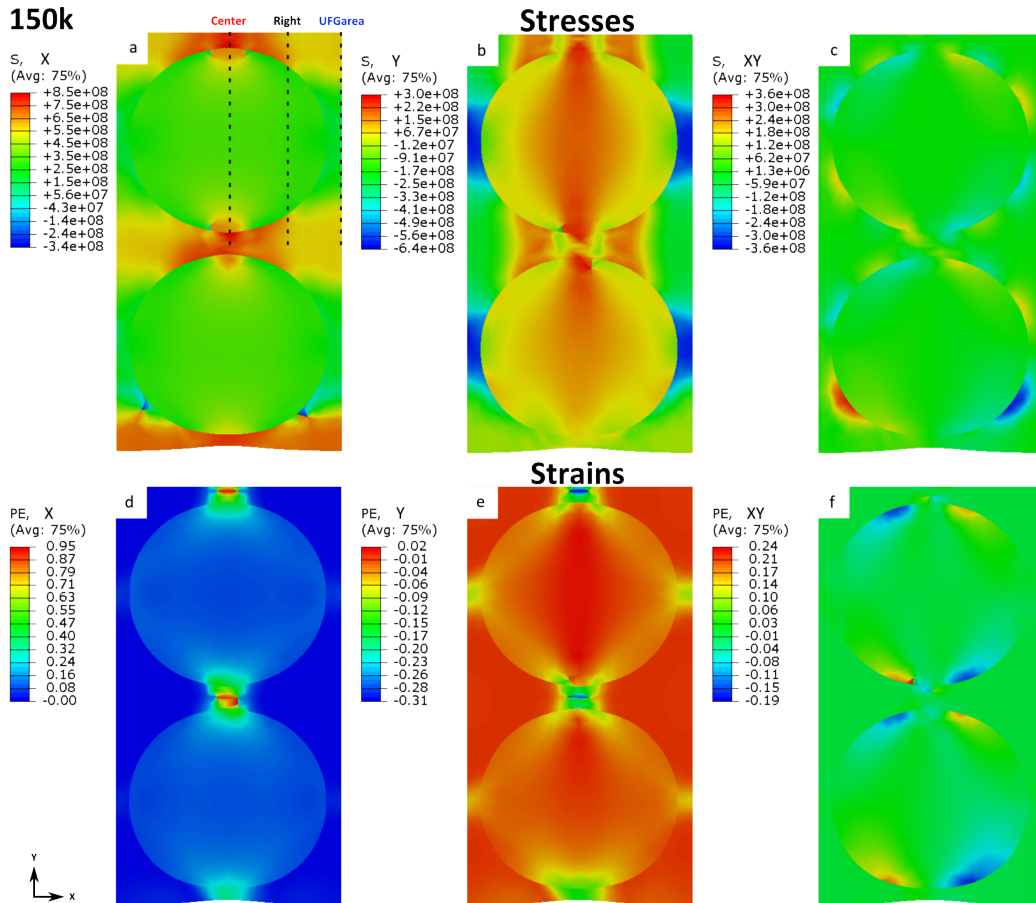


Figure 5.11 stresses and strains for 150k elements in x, y and xy-direction, corresponding to the plots displayed in fig. 5.12.

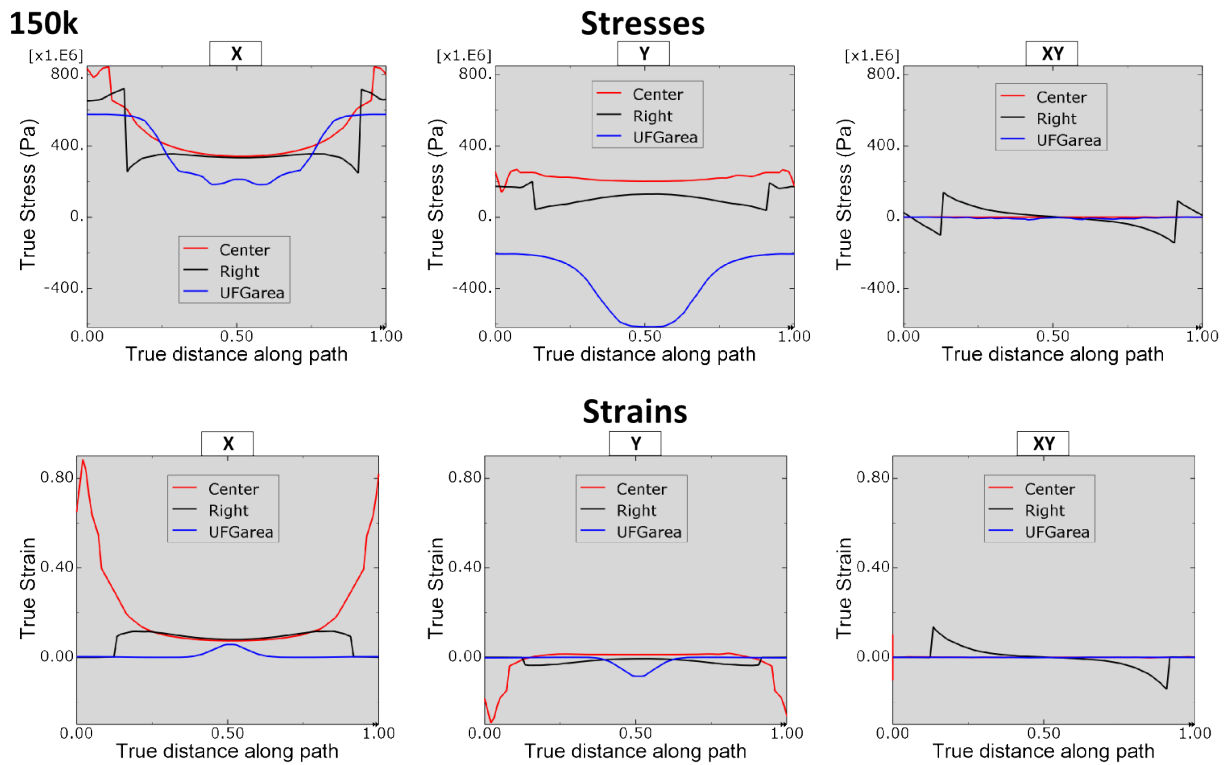


Figure 5.12 stress and strain components for coarse mesh in x, y and xy-direction, corresponding to the imagery presented in fig. 5.11. The plots matches the paths displayed in fig 5.11a.

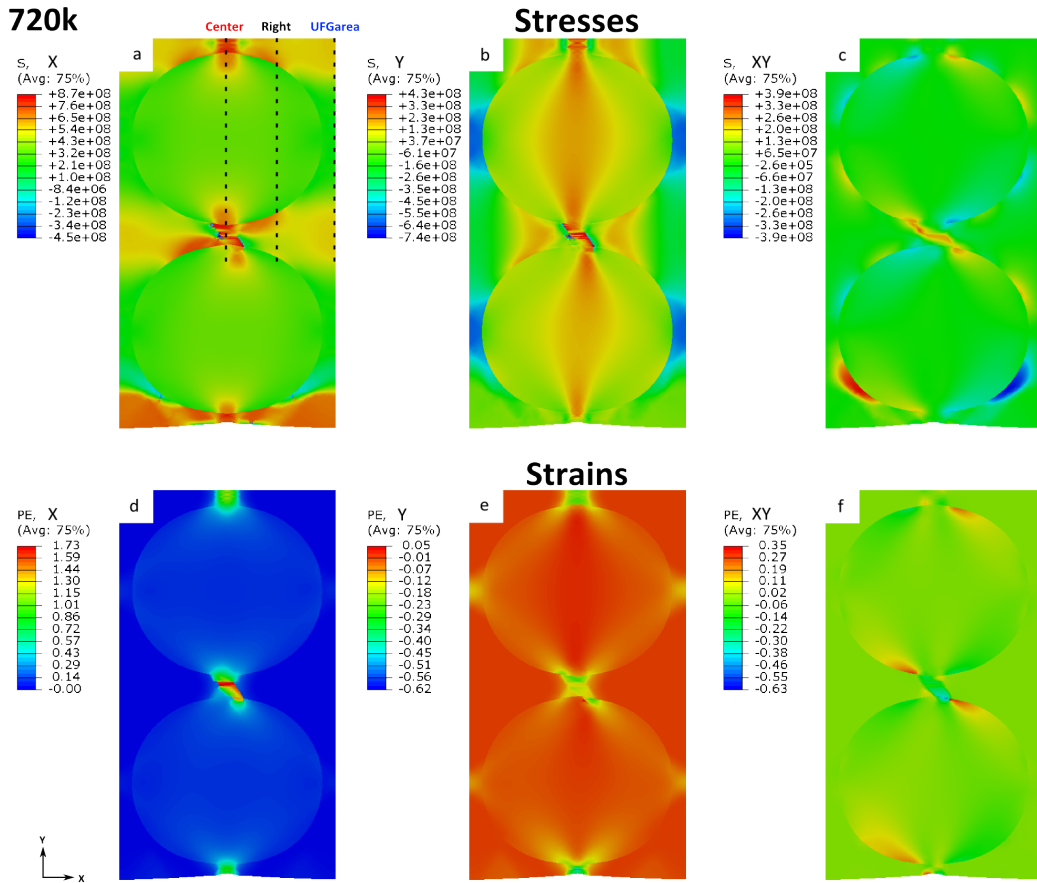


Figure 5.13 stresses and strains for the fine meshed model in x, y and xy-direction. Note the shear stress in (c).

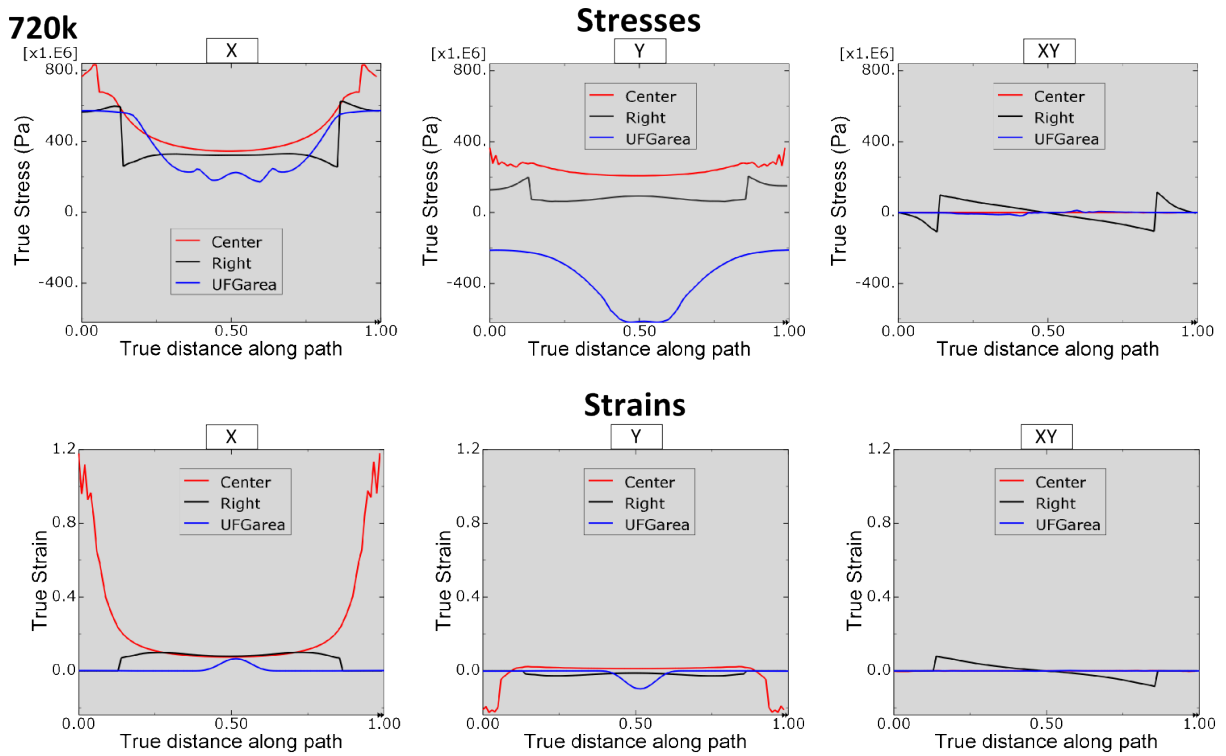


Figure 5.14 corresponding plots for the imagery in fig. 5.13.

5.6 Element Deformation

Severe element deformation occurred during the executed simulations when the models were pulled further and prevented in these cases from providing additional results. It can be noted (fig. 5.15) that less elements seems to allow longer possible total deformation of the model. In (b, e and h) all three variants are pulled to a total of 8% strain, resulting in a maximum stretch of 34% for the coarse mesh while the medium fine and very fine meshed have deformed 104 and 211% respectively in critical areas. At this point the elements are already heavily distorted and the upper limit for these meshes must be around here. Pulling them just slightly longer results in a complete model failure, as displayed in (f and i) at 14 and 12% respectively. The views are representative for the entire cross-section of the model. At 8% or

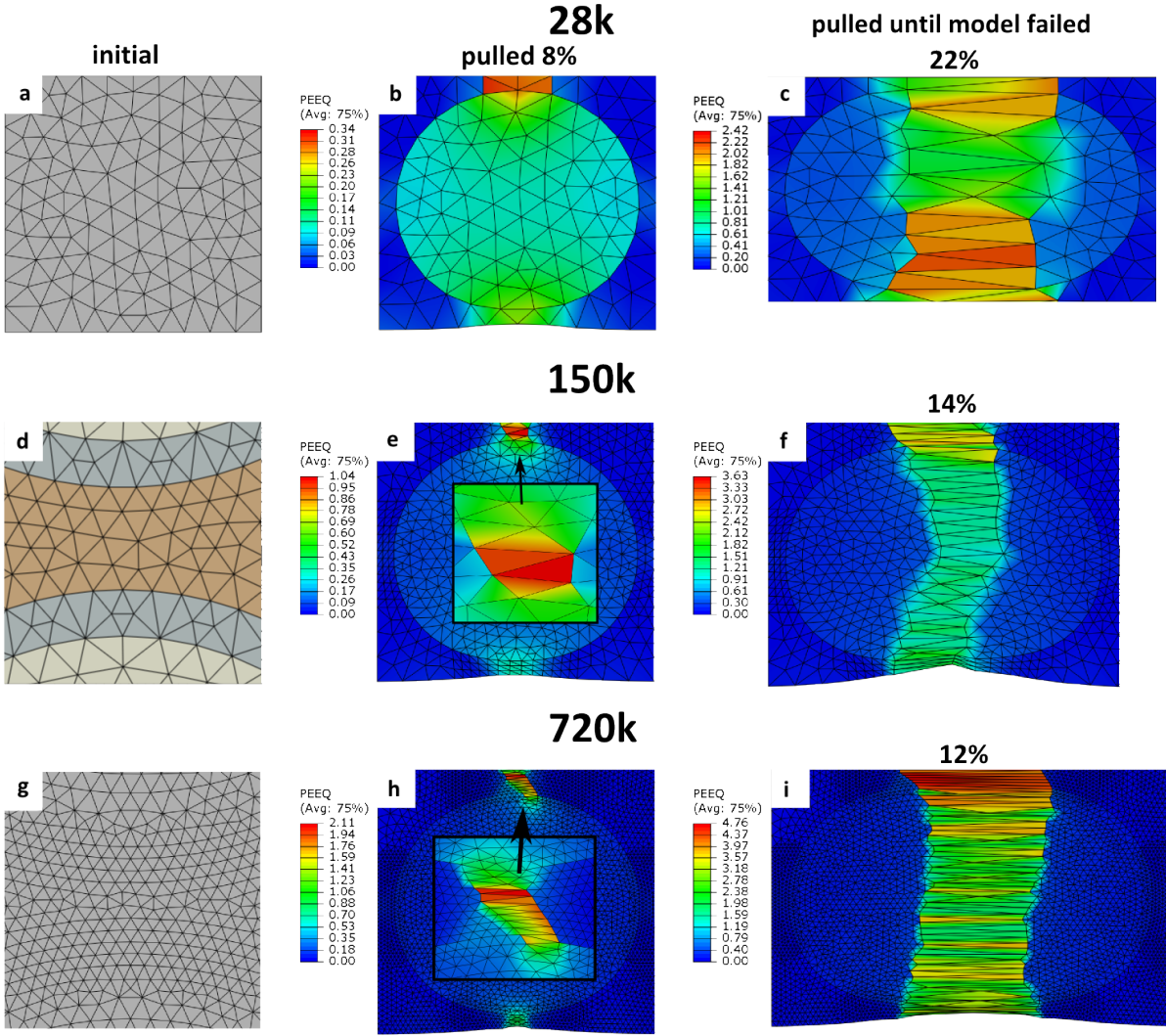


Figure 5.15 element deformation by comparing the different mesh alternatives. A coarse mesh can be pulled further before the model completely fails (c) compared to a finer mesh which fails quite early (f, i).

slightly before, a re-mesh would be needed. Abaqus offers three different techniques to apply at this sort of problem using ALE adaptive meshing, Adaptive remeshing or Mesh-to-mesh solution mapping. Owing insufficient time for this project they were just briefly tested but without improvements in the first two, more of this in future recommendations in chapter 7.

The coarse meshed model on the other hand, could cope with the dislocations quite well and is just slightly deformed at 8% and didn't fail until a total elongation of 22% was applied (fig 5.15c).

5.7 Stress-strain curves

To sum up what has been presented in chapter 5, stress-strain curves are plotted in figure 5.16 and 5.17. In the first set of figures the models have been pulled as long as possible before failure and are compared with another simulation to show what happens just after failure. The latter figure displays the models just before failure.

It can be said that the YS has increased in all three cases from the original (CG) 160 MPa to roughly 290 for the coarse grained and roughly 270 and 250 MPa for the medium fine and very fine mesh respectively. At the same time the UTS has decreased a lot to as highest, for the coarse mesh, approximately 580 MPa while the finer meshes matches just about 530 and 500 MPa. As to compare to the YS achieved by CG and UFG (596 and 751 MPa respectively). Both 28k and 150k elements models exhibit a severe increase in total elongation compared to purely UFG (10%) by approximately 20 and 16% respectively while the finest mesh cope with roughly 11%.

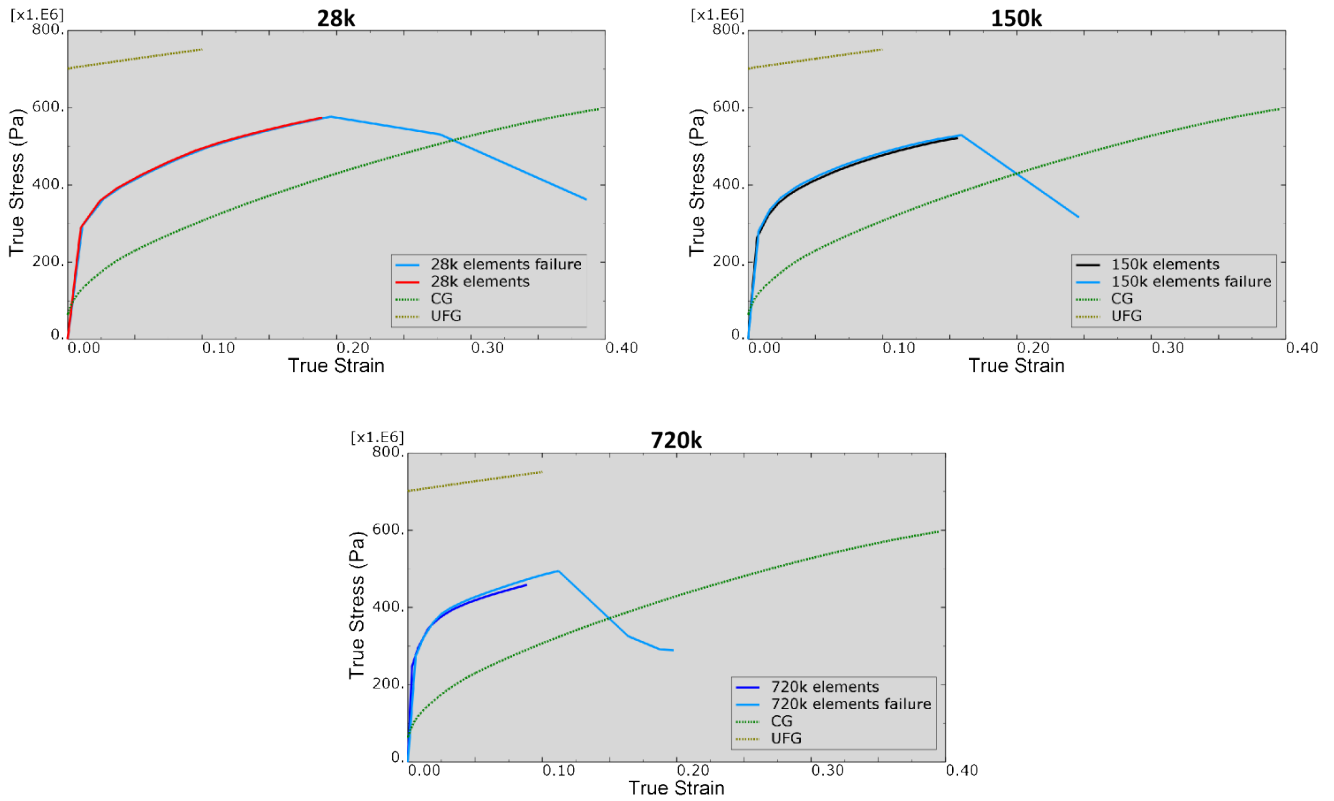


Figure 5.16 stress-strain plots for 28k, 150k and 720k meshed models both slightly before and after failure. It can be noted that the coarser the mesh the longer it can be pulled. Here compared the purely CG and purely UFG.

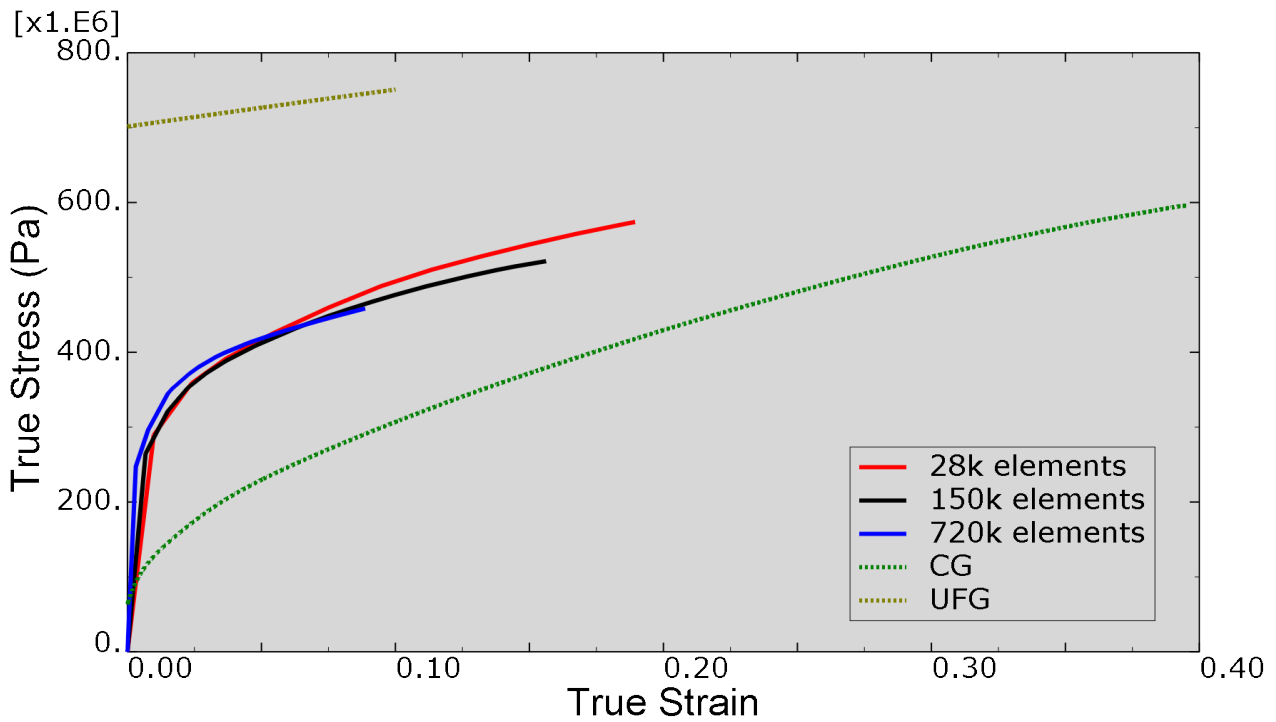


Figure 5.17 final results for the different mesh (28k, 150k, and 720k elements). All three models are pulled as far as possible but just before they fail. Due to sever element deformation and higher resolution, finer mesh equals less total elongation. Pure CG and pure UFG suits as comparison.

5.8 Heterogeneous structure

The random distributed structure with corresponding von Mises stresses and equivalent strains (PEEQ) are displayed in figure 5.18. Contrary to the harmonic structured topology, the same uniform pattern is not present here resulting in an earlier fracture and eventually failure. This is a result of higher stresses, and consequently higher strains, that cumulates rather than scatter across a larger area.

Stress-strain curve for the heterogeneous structure can be viewed in figure 5.19 with a comparison to the coarse meshed harmonic structure. As shown, there is a quite clear advantage for the harmonic structure in both strength and elongation. YS, UTS and uniform elongation have all been reduced to roughly 212 MPa, 530 MPa and 17% respectively. In comparison, the harmonic structure achieved, as mentioned before, 290 MPa, 580 MPa and 20%. A reduction for all three parameters by 27%, 9% and 15% correspondingly.

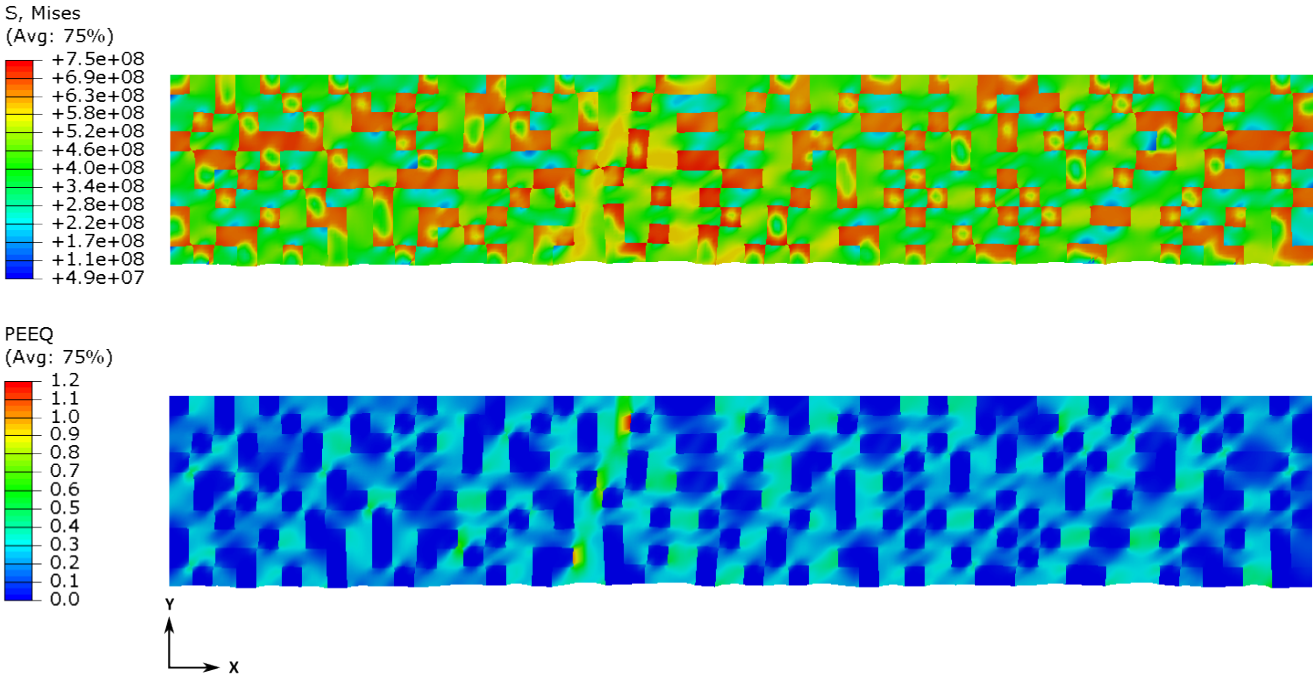


Figure 5.18 von Mises stress and equivalent strains for the heterogeneous structure. The random distributed topology reduces the total elongation of the model.

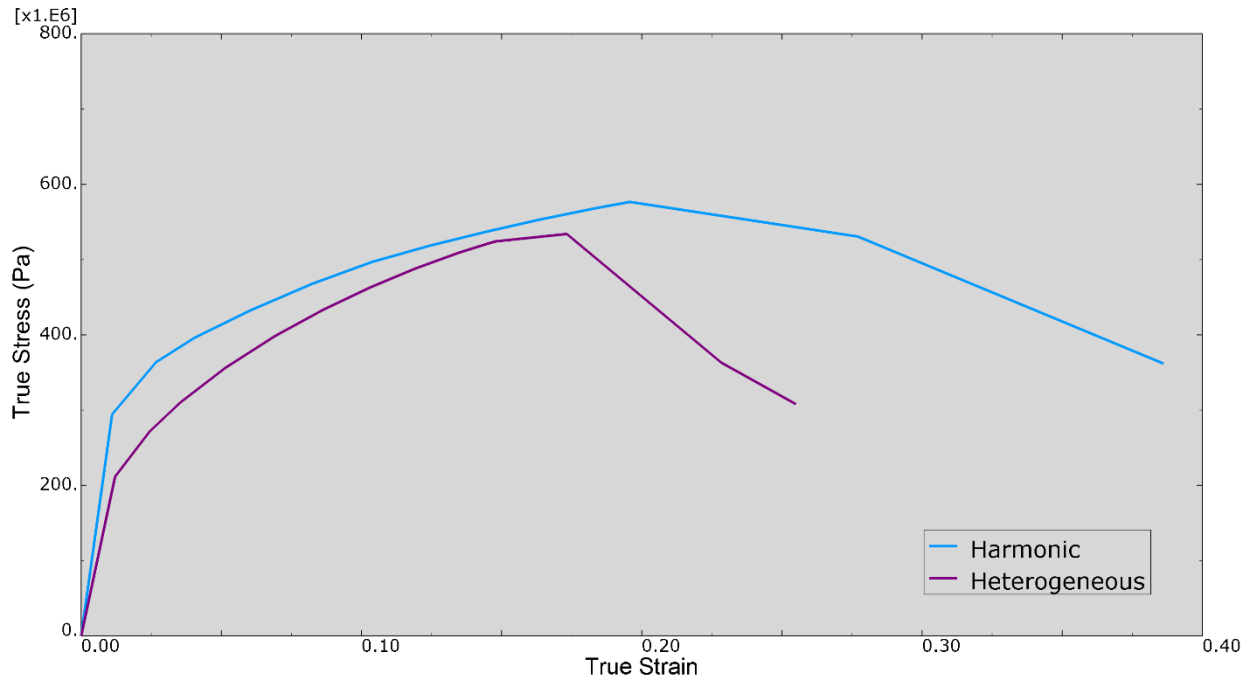


Figure 5.19 advantage of the harmonic structure compared to the heterogeneous one. The latter exhibits poorer results in all three measurements namely YS, UTS and total elongation (212MPa, 530MPa and 17% respectively).

6 Conclusions and Future Work

6.1 Conclusions

FE models of a harmonic structure were successfully created. Owing the two dimensional approach, some restrictions relative the true specimen were faced. The numerical results almost perfectly coincide with the coarse grained experimental outcomes for both the coarse meshed model and the finer alternatives.

The results from the Bimodal harmonic structure imply that there is an advantage for such topology with both increasing yield strength and total elongation when compared to the uniform alternatives. But when considering the UTS, none of the alternatives even reached the same peak as the CG where the finest mesh was worst with 500 MPa, while the coarse meshed model reached approximately 580 MPa. The reason for this should be large element deformation in some critical areas. As a comparison, the model achieved the maxima of 596 MPa when calibrated purely for CG.

The models worked well until the excessive element deformation occurred leading to failure as a consequence. This was most critical for the finer meshes, very likely for two main reasons. Firstly, a finer mesh produces a higher resolution, which might yield larger stresses in critical areas, resulting in large element deformation and eventually failure. Secondly, the single mesh element might simply not cope with the large local deformation owing to its relatively small size compared to the deformed area. Both problems will probably be solved with a local re-mesh. However, due to insufficient time, and after several tries with the two automated re-meshing techniques provided by Abaqus but without any improvements, this was not investigated further.

When considering the model with random distributed grain size topology it was successfully shown that a bimodal harmonic structure outperformed this alternative both in strength and total elongation.

6.2 Future work

As discussed, the model failed very likely after severe element deformation in some local zones. This needs to be solved. *ALE adaptive meshing* and *Adaptive remeshing* techniques were tested in the present project but without success. A more powerful, but time consuming, technique would be the *Mesh-to-mesh solution mapping* technique where the user manually, or by some minor changes in the input file, map the solution from the old to the new mesh. This needs to be done before the elements deforms excessively. The procedure will then be repeated until the stress-strain curve flattens out, probably not more than ten times.

Some scepticism, on the approximation made for the model, was raised after the results had been analysed. If chosen properly, a cross section of the present BCC model could contain purely UFG, which is very unlikely to be the case in the real three dimensional material. Therefore, instead of the uniform pattern displayed in figure 4.3, a FCC-like structure schematically displayed in figure 1.1 was created. This topology would have the benefit of resembling the three dimensional harmonic FCC structure in the material more properly when applied onto two dimensions. Figure 6.1 demonstrates the advantage for strength and elongation of the two dimensional FCC-like structure compared to the BCC results presented in this dissertation. Depending on the aim for future research, this could be an alternative choice.

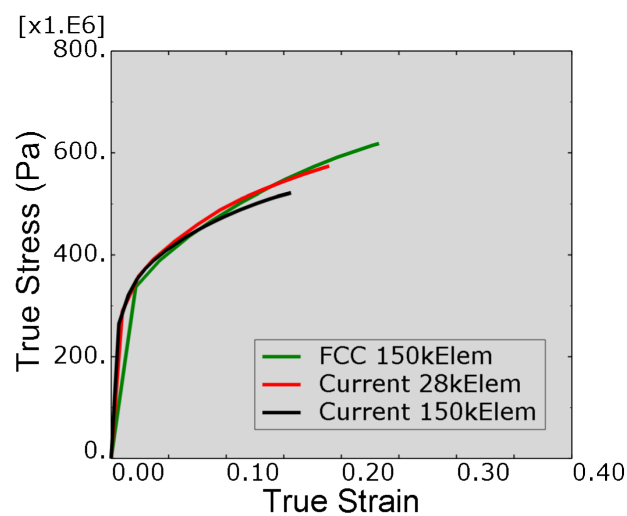


Figure 6.1 advantage of FCC-like structure compared to the results presented in this dissertation. Comparing the FCC-like (green) with the current (black) structure (both 150k elements) shows a distinct advantage for the first in total elongation as well as in strength.

References

- [1] C. Sawangrat, S. Kato, D. Orlov and K. Ameyama, “Harmonic-structured copper: performance and proof of fabrication concept bases on severe plastic deformation of powders,” *Journal of Materials Science*, pp. 6579-6585, 2014.
- [2] D. Orlov, H. Fujiwara and K. Ameyama, “Obtaining Copper with Harmonic Structure for the Optimal Balance of Structure-Performance Relationship,” *Materials Transactions*, vol. 54 No.9, pp. 1549-1553, 2013.
- [3] Z. Zhang, S. K. Vajpai, D. Orlov and K. Ameyama, “Improvement of mechanical properties in SUS304L steel through the control of bimodal microstructure characteristics,” *Materials Science & Engineering A*, pp. 106-113, 2014.
- [4] H. Fujiwara, T. Kawabata, M. Hiroyuki and K. Ameyama, “Mechanical Properties of Harmonic Structured Composite with Pure Titanium and Ti-48at%Al Alloy by MM/SPS Process,” *Materials Transactions*, pp. 1619-1623, 2013.
- [5] O. P. Ciuca, M. Ota, S. Deng and K. Ameyama, “Harmonic Structure Design of a SUS329J1 Two Phase Stainless Steel and Its Mechanical Properties,” *Materials Transactions*, vol. 54, pp. 1629-1633, 2013.
- [6] M. Ota, K. Shimojo, S. Okada, S. Vajpai and K. Ameyama, “Harmonic Structure Design and Mechanical Properties of Pure Ni Compact,” *Journal of Powder Metallurgy & Mining*, 2014.

- [7] H. Yu, I. Watanabe and K. Ameyama, "Deformation Behavior Analysis of Harmonic Structure Materials by Multi-Scale Finite Element Analysis," *Advanced Materials Research*, vol. 1088, pp. 853-857, 2014.
- [8] N. Ottosen and H. Petersson, *Introduction to the FINITE ELEMENT METHOD*, Prentice Hall Europe, 1992.
- [9] N. S. Ottosen, M. Ristinmaa and C. Ljung, Hållfasthetslära, Allmänna tillstånd, 1:1 ed., The Authors and Studentlitteratur, 2007.
- [10] 3ds, *Abaqus Theory Manual 6.12*, 6.12 ed.
- [11] 3. D. Systems, "The 3DEXPERIENCE company," 3 Dassault Systems, [Online]. Available: <http://www.3ds.com/products-services/simulia/products/abaqus/abaqusstandard/>. [Accessed 12 04 2016].
- [12] 3ds, *Abaqus 6.12 Analysis User's Manual*, 6.12 ed., vol. 5.
- [13] D. Roylance, "Stress-strain curves," Cambridge, 2001.
- [14] 3ds, *Abaqus/CAE User's Manual*, Abaqus 6.12 ed.
- [15] C. Ljung, N. S. Ottosen and M. Ristinmaa, *Introduktion till Hållfasthetslära*, Enaxliga Tillstånd, 1:1 ed., The Authors and Studentlitteratur, 2007.

Appendix A, Abaqus input file

The nodes, elements and sets have been cut and replaced by a few dots to fit into four pages. The alternative would constitute of another 1000 pages. It shall be noted that this is the coarse meshed model. If the entire input file is desired for this or for the finer meshed models, please feel free to contact the author.

```
*Heading
** Job name: 5x25-28kElem-noY-P5 Model name: Model-1
** Generated by: Abaqus/CAE 6.12-3
*Preprint, echo=NO, model=NO, history=NO, contact=NO
**
** PARTS
**
*Part, name=Circles-5x25-Verify
*Node
    1,          23.5,          3.5
    2,          24.5,          3.5
    3,          24.5,          4.5
    4,          23.5,          4.5
    5,          24.,          4.43701935
    .
    .
    .
    14452,      21.0606098, -0.0507882126
    14453,      21.2279835, -0.167900413
    14454,      20.9802494, -0.0912078843
    14455,      20.9540977, -0.16417022
    14456,      20.7788982, -0.164602742
*Element, type=CPS3
    1,  260,  304,  259
    2,  5430,  263,  264
    3,  5425,  305,  261
    4,  268,  311,  310
    5,  5427,  272,  273
    .
    .
    .
    28306,  14454,  14444,  14452
    28307,  14455,  14429,  14448
    28308,  14455,  14448,  14444
    28309,  14456,  14430,  14410
    28310,  14456,  14429,  14451
*Nset, nset=Circle
    5,  6,  9,  10,  13,  14,  17,  19,  25,
    27,  29,  31,  33,  36,  38,  40
    .
    .
    .
    14449,  14450,  14451,  14452,  14453,  14454,  14455,  14456
*Elset, elset=Circle
```

```

    92,    93,    94,    95,    96,    97,    98,    99,   100,
101,   102,   103,   104,   105,   106,   107
.
.
28304, 28305, 28306, 28307, 28308, 28309, 28310
*Nset, nset=Plate
    1,    2,    3,    4,    5,    6,    7,    8,    9,
10,   11,   12,   13,   14,   15,   16
.
.
14332, 14333, 14334, 14390, 14391, 14392, 14393, 14394, 14395,
14396, 14397, 14398, 14399, 14400, 14401
*Elset, elset=Plate
    1,    2,    3,    4,    5,    6,    7,    8,    9,
10,   11,   12,   13,   14,   15,   16
.
.
28161, 28162, 28163, 28164, 28165, 28166, 28167, 28168, 28169,
28170, 28171, 28172, 28173, 28174, 28175
** Section: Plate
*Solid Section, elset=Plate, controls=EC-1, material="Material-Ni
UFG extrapolated"
1.,
** Section: Circle
*Solid Section, elset=Circle, controls=EC-1, material="Material-Ni
CG Interpolated"
1.,
*End Part
**
**
** ASSEMBLY
**
*Assembly, name=Assembly
**
*Instance, name=Circles-5x25-Verify-1, part=Circles-5x25-Verify
*End Instance
**
*Nset, nset=_PickedSet15897, internal, instance=Circles-5x25-Verify-
1
    243, 244, 246, 248, 250, 252, 5213, 5214, 5215, 5216, 5217,
5218, 5219, 5220, 5221, 5257
.
.
*Elset, elset=_PickedSet15897, internal, instance=Circles-5x25-
Verify-1
    24120, 24136, 24137, 24138, 24159, 24168, 24170, 24171, 24172,
24191, 24340, 24356, 24357, 24358, 24379, 24388
.
.
*Nset, nset=_PickedSet15898, internal, instance=Circles-5x25-Verify-
1
    2,    3,   263,   264,   265,   266,   267,   268,   269,
270,   271, 12983, 12997, 12998, 12999, 13000
.
.

```

```

*Elset, elset=_PickedSet15898, internal, instance=Circles-5x25-
Verify-1
    2,    37,    38,    40,    41,    42,    43,    44,    45,
77, 25236, 25271, 25272, 25273, 25274, 25275
    .
    .
*Nset, nset=_PickedSet15899, internal, instance=Circles-5x25-Verify-
1
    3,    4,    8,    12,    16,    24,    35,    46,    57,    68,    79,
90, 101, 112, 123, 134
    .
    .
*Elset, elset=_PickedSet15899, internal, instance=Circles-5x25-
Verify-1
    5,    38,    47,    48,    49,    50,    51,    52,    53,
86, 366, 399, 408, 409, 410, 411
    .
    .
*End Assembly
**
** ELEMENT CONTROLS
**
*Section Controls, name=EC-1, DISTORTION CONTROL=NO
1., 1., 1.
**
** MATERIALS
**
*Material, name="Material-Ni CG Interpolated"
*Density
8890.,
*Elastic
2.1e+11, 0.31
*Plastic
6.34617e+07, 0.
6.57839e+07, 0.0002
6.80336e+07, 0.0004
7.02136e+07, 0.0006
7.23265e+07, 0.0008
    .
    .
    .
5.9557e+08, 0.3942
5.95626e+08, 0.3944
5.95676e+08, 0.3946
5.9572e+08, 0.3948
5.95759e+08, 0.395
*Material, name="Material-Ni UFG extrapolated"
*Density
8890.,
*Elastic
2.1e+11, 0.31
*Plastic
7.01442e+08, 0.
7.01545e+08, 0.0002
7.01648e+08, 0.0004

```

```

7.01751e+08, 0.0006
7.01853e+08, 0.0008
.
.
.
7.5039e+08, 0.0992
7.50485e+08, 0.0994
7.50579e+08, 0.0996
7.50673e+08, 0.0998
7.50768e+08, 0.1
**
** BOUNDARY CONDITIONS
**
** Name: LeftSym Type: Symmetry/Antisymmetry/Encastre
*Boundary
_PickedSet15897, XSYMM
** Name: TopSym Type: Symmetry/Antisymmetry/Encastre
*Boundary
_PickedSet15899, YSYMM
** -----
**
** STEP: Step-1
**
*Step, name=Step-1, nlgeom=YES, inc=5000
*Static
0.001, 1., 1e-10, 0.1
**
** BOUNDARY CONDITIONS
**
** Name: RightPull Type: Displacement/Rotation
*Boundary
_PickedSet15898, 1, 1, 5.
_PickedSet15898, 6, 6
*Adaptive Mesh Controls, name=Ada-1
1., 0.
**
** OUTPUT REQUESTS
**
*Restart, write, number interval=1, time marks=NO
**
** FIELD OUTPUT: F-Output-1
**
*Output, field, number interval=20, time marks=NO
*Node Output
CF, RF, U
*Element Output, directions=YES
LE, PE, PEEQ, PEMAG, S, STATUS
**
** HISTORY OUTPUT: H-Output-1
**
*Output, history, variable=PRESELECT
*End Step

```

Appendix B, MATLAB code

Below follows the MATLAB code devoted for interpolation of raw, coarse grained, experimental data where A is a matrix containing all the stresses and strains.

```
A=  
[60398909.1975205 0.00000000000000000000  
62406190.9659776 0.00006566619961283  
63594109.1159323 0.0001626606602601  
64378519.6766914 0.00022811662546616  
65386300.7559127 0.00032469626131234  
.  
.  
.  
595303448.286595 0.393037805321045  
595084389.180924 0.393049392081516  
595440268.217519 0.393061113435158  
595164113.897032 0.393064346887847  
595377008.221281 0.393073508280355];
```

```
[p] = polyfit(A(:,2),A(:,1),19)
```

```
y = polyval(p,A(:,2))
```

```
figure(1)  
plot(A(:,2),A(:,1),'rx')  
hold on  
plot(A(:,2),y)  
hold on
```

```
x = 0:0.0002:0.4;  
y = polyval(p,x)
```

```
By=[y] '  
Bx=[x] '  
format long
```

MATLAB code devoted for extrapolation of coarse grained material data resulting in the ultrafine grained data.

```
Stress=
[26828927.470826
27547370.1398117
28210245.5626047
.
.
592489730.570508
592663905.83067
592588066.546349];

Strain=
[4.68418928573437E-06
0.0000612823224566471
0.0000934798308811379
.
.
0.390580265916147
0.390563349170174
0.390557123735621
];

[p]=polyfit(log(Strain),log(Stress),1);

A=exp(p(2));

b=p(1);

figure(1)

v=[0:0.001:1]';

sigma=(A.*v.^b);

B=plot(v,sigma,Strain,Stress);
```